

## Geochemistry, Geophysics, Geosystems



#### RESEARCH ARTICLE

10.1029/2025GC012629

#### **Key Points:**

- We report never-before electrical conductivity measurements during deformation at high pressures (1 GPa) in a Griggs apparatus
- Under upper-mantle conditions, stress, and strain impact electrical conductivity in contrasting manners in the elastic and plastic regimes
- For a dunite, the conductivity varies within an order of magnitude during elastic (un)loading, requiring reinterpreting the electrical profiles

#### **Supporting Information:**

Supporting Information may be found in the online version of this article.

#### Correspondence to:

T. P. Ferrand, ferrand@geologie.ens.fr

#### Citation:

Ferrand, T. P., Précigout, J., Sifré, D., Vrijmoed, J. C., John, T., Savoie, F., et al. (2025). Electrical conductivity during controlled deformation at upper-mantle conditions: First experimental achievements in a Griggs-type apparatus. *Geochemistry, Geophysics, Geosystems*, 26, e2025GC012629. https://doi.org/10.1029/2025GC012629

Received 28 AUG 2025 Accepted 25 OCT 2025

#### **Author Contributions:**

Conceptualization: Thomas P. Ferrand Data curation: Thomas P. Ferrand, Jacques Précigout

Formal analysis: Thomas P. Ferrand Funding acquisition: Thomas P. Ferrand, Timm John

Investigation: Thomas P. Ferrand, Jacques Précigout, Johannes C. Vrijmoed Methodology: Thomas P. Ferrand, David Sifré, Frédéric Savoie, Rémi Champallier, Fabrice Gaillard

© 2025 The Author(s). Geochemistry, Geophysics, Geosystems published by Wiley Periodicals LLC on behalf of American Geophysical Union.

This is an open access article under the terms of the Creative Commons Attribution License, which permits use, distribution and reproduction in any medium, provided the original work is properly cited.

# Electrical Conductivity During Controlled Deformation at Upper-Mantle Conditions: First Experimental Achievements in a Griggs-Type Apparatus

Thomas P. Ferrand<sup>1,2,3,4</sup>, Jacques Précigout<sup>1</sup>, David Sifré<sup>1</sup>, Johannes C. Vrijmoed<sup>2</sup>, Timm John<sup>2</sup>, Frédéric Savoie<sup>1</sup>, Rémi Champallier<sup>1</sup>, and Fabrice Gaillard<sup>1</sup>

<sup>1</sup>Institut des Sciences de la Terre d'Orléans, CNRS UMR 7327, BRGM, Université d'Orléans, Orléans, France, <sup>2</sup>Institute of Geological Sciences, Freie Universität Berlin, Berlin, Germany, <sup>3</sup>Institut Langevin, ESPCI Paris, CNRS UMR 7585, Université PSL, Paris, France, <sup>4</sup>Laboratoire de Géologie de l'Ecole normale supérieure, CNRS UMR 8538, Université PSL, Paris, France

**Abstract** Electrical conductivity measurements on well-characterized materials in the laboratory allow accurate interpretations of high-conductivity anomalies within the lithosphere and asthenosphere, both affected by substantial deformation over geological times. However, only a few experiments so far have measured rock conductivity during controlled deformation at high pressures (≥1 GPa) and temperatures (500–1,000°C). Here, we report the first successful deformation experiments performed in a new-generation Griggs-type apparatus adapted for electrical measurements. As a proof of concept, one successful experiment was conducted on Carrara marble at a confining pressure of 1 GPa and temperatures of 500, 650, and 800°C. Three other experiments were then performed at the same pressure to explore the electrical conductivity of Åheim dunites at 500, 650, and 800°C, respectively. Our results show very different electrical responses in the elastic and plastic regimes. Stress and strain can significantly impact the electrical conductivity of peridotites by changing the thickness, number, or geometry of grain boundaries. At fixed P-T conditions, the electrical conductivity varies within an order of magnitude during elastic loading and unloading, which motivates reappraisal of interpretations of electrical anomalies in mantle rocks, at least in tectonically active regions. Upon additional development to achieve deformation up to 4 GPa (≈120 km depth), the design presented here opens a fully new research field, which will help to more deeply understand electrically conductive anomalies in rocks under stress at depth, notably within the lower crust, upper mantle and subducting slabs.

Plain Language Summary Natural features, such as seismogenic faults, plate interfaces, or magmatic provinces, can show abnormally high conductivity values at depth, as revealed by magnetotellurics. These anomalies are interpreted by the presence of conductive materials, such as brines, melts, or water-bearing rocks. Several parameters such as temperature and composition can influence the electrical conductivity of rocks. In most rocks, grain boundaries are much more conductive than mineral phases due to their more heterogeneous composition. Water can be trapped at grain boundaries in the form of adsorbed fluids or ions bonded to crystal lattices, increasing the number of charge carriers. Consequently, the shape, thickness, and water content of grain boundaries control the ability of electrons to travel through. Until now, deep conductive anomalies have been interpreted by changes in mineralogy, water content, or partial melting. For the first time, we show that deformation at high pressures and temperatures can significantly modulate electrical conductivity values by squeezing or relaxing grain boundaries and forming new ones.

#### 1. Introduction

Laboratory measurements of electrical conductivity have been extensively used by geophysicists and planetary scientists to investigate the nature and evolution of rocks for several decades (e.g., Ferrand, 2020; Ferrand & Chin, 2023; Gaillard et al., 2008; Li et al., 2023; Unsworth et al., 2005; Zhang & Yoshino, 2020). They particularly allow to separately investigate the parameters controlling the conductivity variations deduced from magnetotelluric (MT) studies (e.g., Ferrand & Chin, 2023; Gaillard, 2004; Pommier et al., 2018; Sifré et al., 2014; Zhang & Yoshino, 2020), documenting strong lithospheric anomalies of electrical conductivity, so far attributed to static properties related to rock fabric and deformation features (e.g., Baba et al., 2006; Börner et al., 2018; Evans et al., 2005; Naif et al., 2013; Pommier et al., 2018). However, most in situ electrical measurements have been performed in static conditions, that is, without considering the direct in situ effect of deformation on either

15252027, 2025, 11, Downloa

Project administration: Timm John, Fabrice Gaillard Resources: David Sifré, Johannes C. Vrijmoed, Timm John, Frédéric Savoie, Rémi Champallier, Fabrice Gaillard Software: Johannes C. Vrijmoed, Fabrice Gaillard Supervision: Timm John, Fabrice Gaillard Validation: Jacques Précigout, David Sifré, Fabrice Gaillard Visualization: Thomas P. Ferrand, Jacques Précigout Writing - original draft: Thomas P. Ferrand Writing - review & editing: Thomas P. Ferrand, Jacques Précigout, David Sifré, Johannes C. Vriimoed, Timm John,

Frédéric Savoie, Rémi Champallier,

Fabrice Gaillard

natural or synthetic rocks. Dynamic conditions may yet involve the percolation of conductive fluids, transient stress-induced states of grain boundaries impacting the distribution of electrical charges, or a combination of both phenomena. For instance, various systems such as the magmatic network of the Mount St Helens (Hill et al., 2009) or the East Pacific Rise (Key et al., 2013) are characterized by high-conductivity anomalies that can reach >1 S m<sup>-1</sup>. Although such conductive anomalies are commonly attributed to the suspected presence of connected melts (Gaillard, 2004; Key et al., 2013; Naif et al., 2013), volatiles or fluids (e.g., Karaş et al., 2020; Karato, 1990, 2006; Türkoğlu et al., 2008), some could rather involve a more complex combination of physicochemical processes (e.g., underplating: Ferrand, 2020). Therefore, it is crucial to measure the effect of deformation on electrical conductivity. Although several attempts have been carried out in the past (e.g., Caricchi et al., 2011; Zhang & Yoshino, 2020; Zhang et al., 2014), how deformation can impact electrical conductivity remains poorly documented today at pressures and temperatures representative of the deep lithosphere.

Depending on the context, high conductivity values may suggest diverse origins, including widespread weakening by fluids (e.g., Türkoğlu et al., 2008), the presence of connected melt networks (Hill et al., 2009; Key et al., 2013), or geothermal fields (e.g., Bertrand et al., 2013). Beneath the East Pacific Rise, interconnected melt would form a grain-boundary network below the ridge axis due to percolation from the partially molten asthenosphere (Key et al., 2013). In contrast, offshore Nicaragua, an anisotropic anomaly is interpreted as conductive channels in the deep lithosphere (Naif et al., 2013), which may correspond to the fossilized trace of the lithosphere-asthenosphere boundary (LAB; Ferrand, 2020). For a melt-bearing rock to become conductive, the melt must be connected (e.g., Gaillard et al., 2008; Sifré et al., 2014). Stress-driven melt segregation can lead to large-scale melt redistribution at the LAB (Holtzman & Kendall, 2010; Holtzman et al., 2003, Takei & Holtzman, 2009; Zhang et al., 2014), eventually fossilized as solid-state conductive features (Ferrand, 2020).

The effect of deformation on electrical conductivity has been mostly explored in low-pressure apparatuses so far. This includes deformation experiments below 0.5 GPa, highlighting stress and strain as significantly impacting rock conductivity (Glover et al., 1996; Jouniaux et al., 2006; Lazari et al., 2024), as well as Paterson-type experiments ( $\leq$ 0.7 GPa) that allowed reproducing natural conductivity anomalies characterized by substantial anisotropy (Caricchi et al., 2011). Torsion experiments at 0.3 GPa and strain rates up to  $1.2 \times 10^{-5}$  s<sup>-1</sup> (Caricchi et al., 2011) contributed to explain the anisotropic nature of electrical conductivity anomalies in the deep oceanic lithosphere, as well as the distribution of seamounts (e.g., Ferrand, 2020; Naif et al., 2013) and chemical variations along mid-ocean ridges (e.g., Le Roux et al., 2006; Niu et al., 2002). However, such a pressure of 0.3 GPa is equivalent to a depth of around 10 km only (upper/middle crust), which is not representative for most of the deformation conditions in the lithosphere, the thickness of which may far exceed 100 km.

More recently, shear tests have been performed in a D-DIA (deformation-DIA) apparatus adapted for deformation of thin gouges (0.4–0.8  $\times$  2.6 mm, i.e. 1–2  $\mu$ m<sup>3</sup>) at strain rates up to 8.10<sup>-5</sup> s<sup>-1</sup> (Kawano et al., 2012; Zhang & Yoshino, 2020; Zhang et al., 2014). Due to a specific design, these experiments allowed shearing sub-millimetric gouge samples at a pressure of 1 GPa, which is well adapted to study melt connectivity in the oceanic asthenosphere (Zhang & Yoshino, 2020). However, these simple-shear experiments are only adapted for the deformation of tiny gouges, with a limited range of strain rates not higher than 4  $\times$  10<sup>-5</sup> (Zhang et al., 2014) or 8.13  $\times$  10<sup>-5</sup> s<sup>-1</sup> (Zhang & Yoshino, 2020). Moreover, to date, no design has been implemented to deform large samples (>cm) at  $\geq$ 1 GPa of confining pressure, which is required to better understand high-conductivity anomalies in the lithosphere, for instance to investigate melt segregation and percolation processes.

In recent years, experimental petrology has benefited from the development of a new-generation solid-medium Griggs-type apparatus (Précigout et al., 2018), which can be described as a piston-cylinder with an additional piston for deformation. Modified after the Harry W. Green's design (H. W. Green & Borch, 1989), this new-generation apparatus consists of an evolved version of the deformation rig developed by David T. Griggs from the 60s (Griggs, 1967), then modified by Jan and Terry Tullis in the 70'-80' (Tullis & Tullis, 1986), and implemented in numerous Universities. Thanks to a substantial number of deformation experiments, the Griggs-type deformation apparatuses provided unequivocal data supporting new discoveries in the fields of petrology, rock mechanics, rock physics and earthquake physics (e.g., Burnley & Green, 1989; Gasc et al., 2022; H. W. Green & Borch, 1989; H. W. Green & Houston, 1995; H. W. Green et al., 1990; Holyoke & Kronenberg, 2010; Moarefvand et al., 2021; Précigout & Stünitz, 2016; Précigout et al., 2017, 2019, 2022; Tullis & Tullis, 1986).

In the present study, we report a new design for in situ electrical conductivity measurements using a new-generation Griggs-type apparatus (Précigout et al., 2018). Focusing on coaxial experiments at high pressure

FERRAND ET AL. 2 of 22

15252027, 2025, 11, Downloaded from https://agupubs.onlinelibrary.wiley.com/doi/10.1029/2025GC012629 by ESPCI ParisTech, Wiley Online Library on [26/11/2025]. See the Term

Figure 1. New-generation Griggs-type apparatus and sample assembly. (a) Drawings of the apparatus, providing a three-dimensional view (top right) and cross-section view with internal details of the rams, pistons, and pressure vessel. (b) Sample assembly as regularly used in the new-generation Griggs-type apparatus, that is, before modifications to perform in situ conductivity measurements.

(up to 4 GPa) for variable strain rates (from  $10^{-7}$  to  $10^{-2}$  s<sup>-1</sup>) and temperatures (up to 1,000°C), such design may help better understanding the diversity of natural factors that should be considered to interpret MT profiles, especially regarding the LAB and electrically conductive layers reported blended or parallel to it (Ferrand & Deldicque, 2021; Naif et al., 2013). It may also be helpful to understand the dynamics of active fault zones, for which MT data report high variability in both location (depth) and anisotropy (e.g., Ingham & Brown, 1998; Kluge et al., 2022; Lemonnier et al., 1999; Unsworth, 2010; Unsworth et al., 2005; Xu et al., 2019).

#### 2. Methods and Materials

#### 2.1. Deformation Apparatus and Modifications of the Sample Assembly

The Griggs-type apparatus is based on the piston-cylinder technology, which involves three metallic platens superposed on several tie bars (Figure 1a). While the pressure vessel and base plate rest on the bottom platen, the two other platens are used to fix the hydraulic rams, independently connected to syringe pumps (Stigma pumps from Sanchez Technologies) and suspended over the pressure vessel. Hydraulic pumps provide a quasi-perfect servo-controlled monitoring (±1 MPa) of the pressure applied to the confining and deformation pistons, respectively, used to increase pressure and generate a differential stress within the water-cooled pressure vessel. In contrast to the "traditional" Griggs-type apparatus, the new-generation apparatus is also equipped with an endload system, consisting of an additional piston connected to the confining ram and applying pressure on the pressure vessel itself to reach a pressure far higher than 1 GPa (Figure 1a). Pressure is further increased together with temperature by the Joule effect thanks to a graphite furnace, which is part of the so-called sample assembly (Figure 1b). Such a heating system has the advantage of being highly reactive—the assembly can be quenched in a couple of seconds—but it does imply vertical and radial temperature gradients that may be significant. For instance, applying a temperature of 900°C (as recorded at the thermocouple tip) to a sample of 15 mm long and 8 mm  $\varnothing$ , numerical simulations predict a radial gradient of  $\simeq 30^{\circ}$ C (i.e.,  $870^{\circ}$ C at the sample center) and a vertical gradient of  $\simeq 70^{\circ}$ C between the tip and center of the sample cylinder (Moarefvand et al., 2021). For a dunite, these radial and vertical temperature gradients would respectively divide the electrical conductivity by  $\approx 2$  and  $\approx 3$ (Gardés et al., 2014).

FERRAND ET AL. 3 of 22

To perform a Griggs experiment, a sample assembly is required (Figure 1b). It consists of (a) a solid confining medium, usually NaCl; (b) a furnace made of a graphite tube in between two pyrophyllite tubes to protect it; (c) a lead piece to homogenize stresses during compaction of the assembly; (d) A top and bottom alumina (or zirconia) pistons to deform the sample; (e) a platinum jacket welded (or bended flat) at both sides around the sample; (f) a tungsten carbide (WC) pedestal; (g) one or two S-type (or K-type) thermocouple(s) as close as possible to the sample with a maximum error of 1°C at the tip of the thermocouple; (h) two copper discs to conduct the electrical current from bottom to top; and (i) two packing rings, that is, metallic anti-extrusion gaskets. In the present study, this "traditional" sample assembly was adapted to measure electrical conductivity during the experiment, which included increasing pressure and temperature (pumping stage), sample deformation and quenching of the assembly. Further technical details about Griggs-type experiments using the new-generation rig can be found in the literature (Précigout et al., 2018).

In order to measure the electrical conductivity of a given sample in the new-generation Griggs apparatus, we took advantage of existing designs successfully applied to the solid-medium piston-cylinder press (Sifré et al., 2014) and to the gas-medium Paterson press (Caricchi et al., 2011). This setup is dedicated to measuring radial conductivity, contrary to other designs in multi-anvil presses measuring axial conductivity (e.g., Ferrand & Chin, 2023). With respect to the "traditional" sample assembly, the base plate, WC pedestal and bottom alumina piston were first drilled along their axis to produce a 2-mm-Ø borehole, so that one wire (protected within a sheath of alumina) was inserted up to the inner electrode. The latter consists of a 2-mm-Ø nickel cylinder inserted along the axis of the sample core drill. A second wire was then inserted through one thermocouple hole (within a mullite sheath) and put in contact with the platinum jacket, here used as the outer electrode (Figure 2). To avoid any shortcut, in this case, the platinum jacket is not closed, but consists of an 18-mm-long tube overlapping both alumina pistons. This adapted design is here referred to as *ElectroGriggs*.

#### 2.2. Starting Material

To test this new design, we used a core-drill of Carrara marble (Figure 3) which has been a reference material for many studies aiming at calibrating deformation apparatuses and exploring deformation processes of mono-phased and homogeneous rocks (Barnhoorn et al., 2004; Bruijn et al., 2011; Paterson & Olgaard, 2000; Pieri et al., 2001; Rybacki et al., 2021). This material is quasi non-porous, highly homogeneous and composed of undeformed CaCO<sub>3</sub> grains of around 150 µm equivalent diameter with a nearly random crystallographic preferred orientation. For a detailed description of the Carrara marble, the readers may refer to the study of Rybacki et al. (2013).

We then used cored cylinders of Åheim dunite to explore the electrical properties of a rock representative of the uppermost mantle (Figure 4). This rock consists of a chlorite-bearing dunite originating from the Ekramsaeter mine near Åheim in Norway. The material deformed in this study (Table 1) has a good correspondence with the ones described by Jackson et al. (1992). Previous studies also indicate that the Åheim dunite is relatively homogeneous with a constant composition, including mainly olivine (average grain size  $\approx 300~\mu m$ ), with up to 10% of pyroxenes, accessory magnetite and 5%–8% of hydrous silicates (Berckhemer et al., 1982; Chopra & Paterson, 1981; Jackson et al., 1992). The latter consists of clinochlore (5–7 vol.%) along with minor serpentine, talc, phlogopite and amphiboles ( $\approx 1~vol.\%$  in total). Clinochlore occurs as oriented platelets with a diameter of 0.3–1 mm and a thickness around 50  $\mu m$ ; it is dispersed rather homogeneously within the olivine matrix, with the tendency to align parallel to a strong foliation in the rock, but it remains disconnected. One may also notice the presence of sodic amphiboles in the vicinity of a phlogopite grain, that is, cation diversity likely due to fertilization by metasomatic fluids. For experiments, the dunite was cored subparallel to the foliation to produce cylinders 15 mm long and 8 mm in diameter (Table 1).

#### 2.3. Deformation Experiment, Data Acquisition and Processing

The electrical conductivity measurements were performed at P = 1.0 GPa for both the Carrara marble and Åheim dunite. While temperature stepping was applied to test our set-up at 500, 650, and 800°C (OR143TF) using Carrara marble (Figure 3), the Åheim dunite has been deformed at fixed temperatures respectively at 500°C (OR93TF), 650°C (OR100TF), and 800°C (OR96TF), as summarized in Figure 5. Once the conductivity stabilized at the imposed P-T conditions (30 min), the piston was advanced at a constant velocity of  $\simeq 1.2 \times 10^{-4}$  mm s<sup>-1</sup> (flow rate of 0.07 ml min<sup>-1</sup>), giving rise to a strain rate of  $\simeq 7 \times 10^{-6}$  s<sup>-1</sup>. The experiments

FERRAND ET AL. 4 of 22

1525/2027, 2025, 11, Downloaded from https://agupubs.onlinelibrary.wiley.com/doi/10.1029/2025GC012629 by ESPCI Parisfrech, Wiley Online Library on [26/11/2025]. See the Terms and Conditions (https://onlinelibrary.wiley.com/terms-and-conditions) on Wiley Online Library for rules of use; OA articles are governed by the applicable Creati

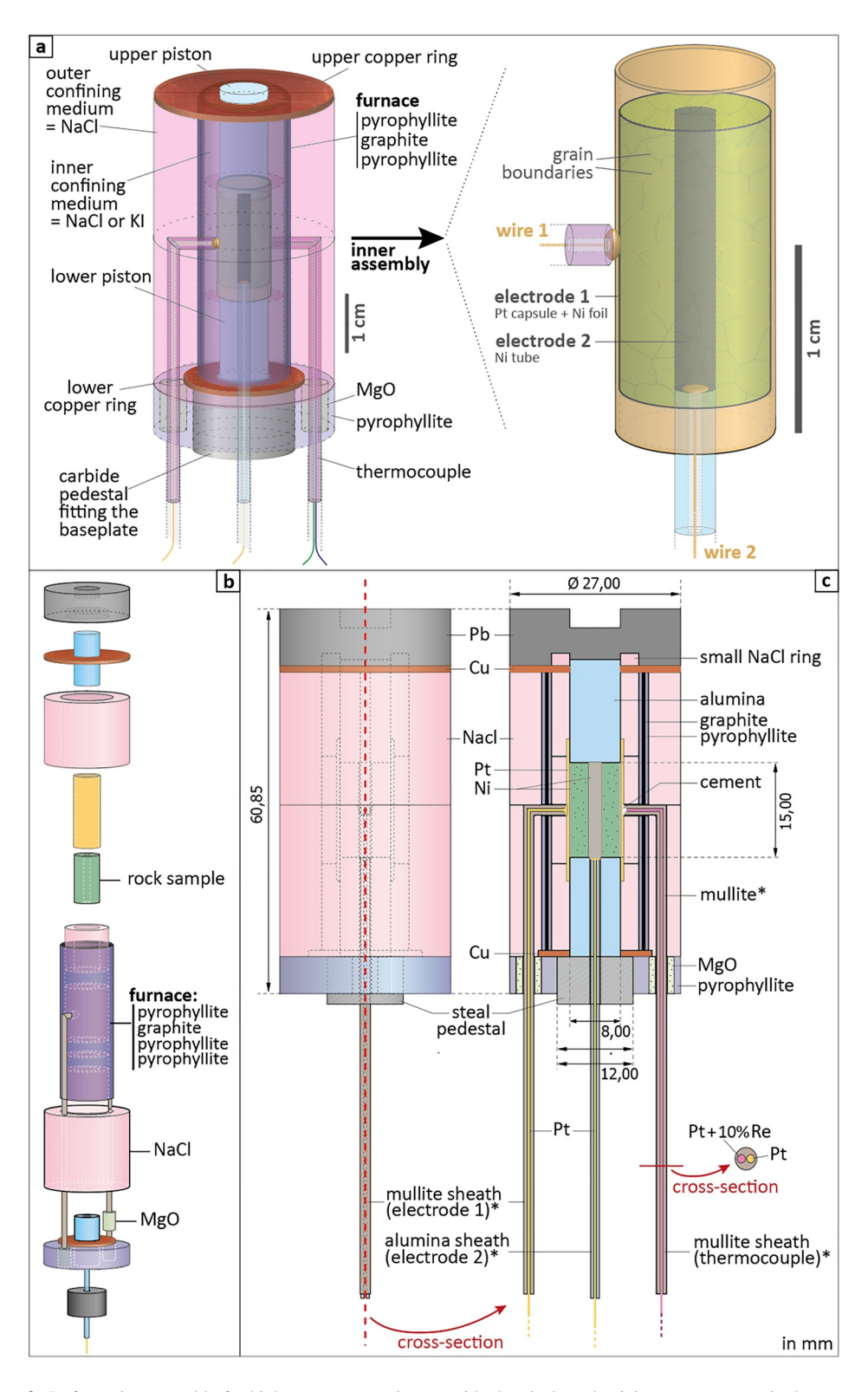


**Figure 2.** Deformation assembly for high-pressure experiments with electrical conductivity measurements in the new-generation Griggs-type apparatus. (a) Sketch of the deformation assembly and closer view of the rock sample and electrodes. Deformation pistons and the protective sheath of wire 2 consist of alumina (blue); Protective sheathes of the thermocouple and wire 1 are made of mullite. (b) Semi-exploded three-quarter view of the assembly; (c) side view of the assembly and section through the electrodes and thermocouple.

FERRAND ET AL. 5 of 22

15252027, 2025, 11, Downloaded from https://agupubs.onlinelibrary.wiley.com/doi/10.1029/2025GC012629 by ESPCI ParisTech, Wiley Online Library on [26/11/2025]. See the Terms

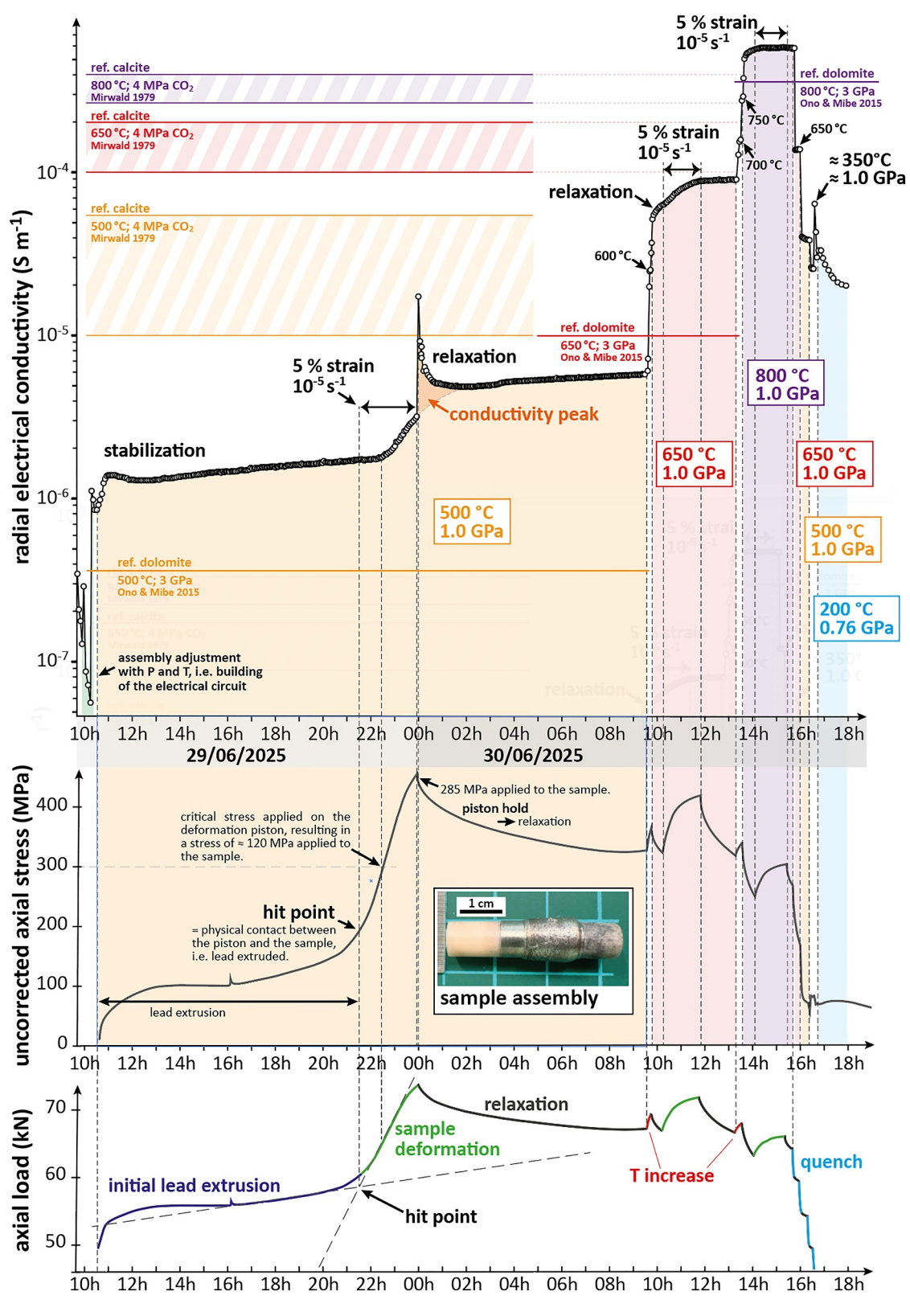
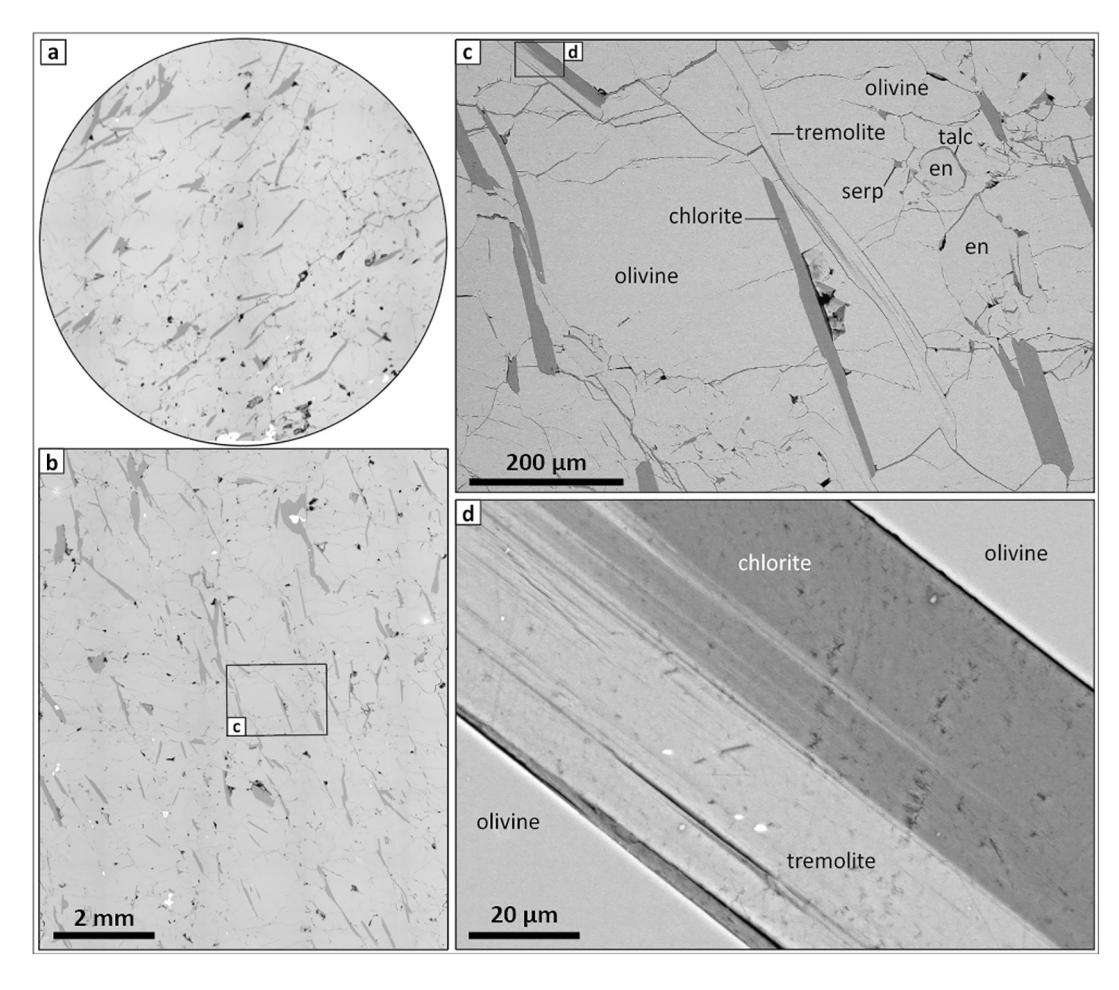


Figure 3.

FERRAND ET AL. 6 of 22

ded from https://agupubs.onlinelibrary.wiley.com/doi/10.1029/2025GC012629 by ESPC1 ParisTech, Wiley Online Library on [26/11/2025]. See the Terms and Conditions (https://onlinelibrary.wiley.



**Figure 4.** Microstructural observations of a subvertical section of the starting material. Backscattered electron image and scanning electron microscopy. (a) horizontal polished surface; (b) vertical polished surface; (c) overview of the main mineralogy of the dunite (located in b) made of olivine, clinochlore (chlorite), enstatite (en) and thin minor phases (e.g., chromite, serpentine, talc, magnetite and phlogopite); (d) detailed view of interlayered chlorite and tremolite (located in c). Black domains correspond to natural porosity and preparation damage.

also include constant-load and/or relaxation steps before quenching the sample to test the impact of differential stress on electrical conductivity in the absence of major strain. The experimental conditions for the three runs are summarized in Table 2.

In situ electrical conductivity measurements were performed every 3–4 min using a 1,260 Solartron Gain-Phase Analyzer, including during the pumping and quenching stages. Impedance spectra were obtained in the frequency range of  $10^{-1}$ – $10^{6}$  Hz. The bulk electrical resistance R is the real part of the impedance obtained for the frequency at which its imaginary part is equal to zero (Figure S1 in Supporting Information S1). In other words, R corresponds to the intersection between the impedance spectrum and the real axis, as previously described (e.g., Gaillard, 2004; Sifré et al., 2014; Zhang & Yoshino, 2020). High resistances ( $R > 500 \,\Omega$ ) induce lower precision, and hence, estimating R from an impedance spectrum may require fitting with an ellipse. For consistency, we here

**Figure 3.** Electrical conductivity of the Carrara marble at high pressure and temperatures in the new-generation Griggs-type apparatus, and impact of deformation. Run OR143TF was performed at 1 GPa containing three main stages at 500, 650, and 800°C, with 5% of deformation at each stage. The electrical conductivity was also recorded during the final cooling. We show the detailed correlation between the experiment and the associated electrical measurements, with comparisons to published data on static experimental measurements demonstrating that the *ElectroGriggs* setup provides accurate electrical measurements. The entire data set is consistent with the literature (measurements in static conditions). Two conductivity peaks are recorded (1) upon mechanical relaxation at 500°C and (2) in the aragonite stability field during the final cooling, suggesting that the calcite-aragonite transition might be seen electrically. Further investigation will help us understand these transient signals.

FERRAND ET AL. 7 of 22

15252027, 2025, 11, Downloaded from https://agupubs.onlinelibrary.wiley.com/doi/10.1029/2025GC012629 by ESPCI ParisTech, Wiley Online Library on [26/11/2025]. See

nditions) on Wiley Online Library for rules of use; OA articles are governed by the applicable Creative Commons Licens

Table 1
Dimensions of the Inner Assembly for Each Experiment on the Åheim Dunite (in mm)

	Dunite sample		Ni tube <sup>a</sup>		Ni foil <sup>b</sup>		Lower piston		Upper piston		Pt capsule	
Run	Height	Radius	Height	Radius	Height	Thickness	Height	Radius	Height	Radius	Height	Radius
OR93TF	14.98	4.00	14.98	1.10	14.0	0.1	14.00	4.00	18.20	4.00	18.00	4.25
OR96TF	15.00	4.00	15.00	1.20	14.0	0.1	13.94	4.00	18.20	4.00	18.00	4.25
OR100TF	15.00	4.00	15.00	1.20	14.0	0.1	13.90	4.00	18.20	4.00	18.00	4.25

<sup>&</sup>lt;sup>a</sup>Inner electrode. <sup>b</sup>Outer electrode.

determine *R* as the intersection between the ellipse and the real axis. Ellipses interestingly highlight that the shape of the measured spectra is shifted from the theoretical shape (circle crossing the origin), revealing minor high-conductivity bodies/pathways, which are not numerous/connected enough to control bulk conductivity.

The electrical conductivity  $\sigma$  is calculated from the resistance R according to the relationship:

$$\sigma = \frac{\ln(r_{\text{ext}}/r_{\text{in}})}{2 \times \pi \times h \times R}$$

where h is sample height,  $r_{\rm ext}$  the radius of rock sample,  $r_{\rm in}$  the radius of the inner electrode ( $r_{\rm in} = 1.1$  mm for OR93TF; Table 1) and R the resistance measured from the complex impedance spectrum. When measuring the electrical conductivity, shortcuts can occur due to either defects or an asymmetry within the deformation assembly. Considering the stability field of the sample-bearing minerals upon heating, clinochlore is also expected to remain stable in all runs, but other phases such as serpentine minerals reach their stability limits at elevated temperatures, which may affect the conductivity (Figure 6). In addition, considering the thermal gradient between the center and tips of the sample, it is possible that some dehydration-induced fluids can percolate during deformation for OR96TF and OR100TF. Furthermore, for the sake of clarity, we only refer to conductivity values assuming progressive extrusion of the Ni inner electrode.

The processed mechanical data and associated electrical data are presented together with stress  $\xi$  as a function of strain  $\varepsilon$  in Figure 6. The initial linear part is defined as the elastic strain, until yielding followed by plastic strain. Although stress accuracy has been estimated at  $\pm 30$  MPa for the conventional Griggs-type apparatus (Holyoke & Kronenberg, 2010; Kido et al., 2016), our experiments have been performed in the new-generation one, accuracy

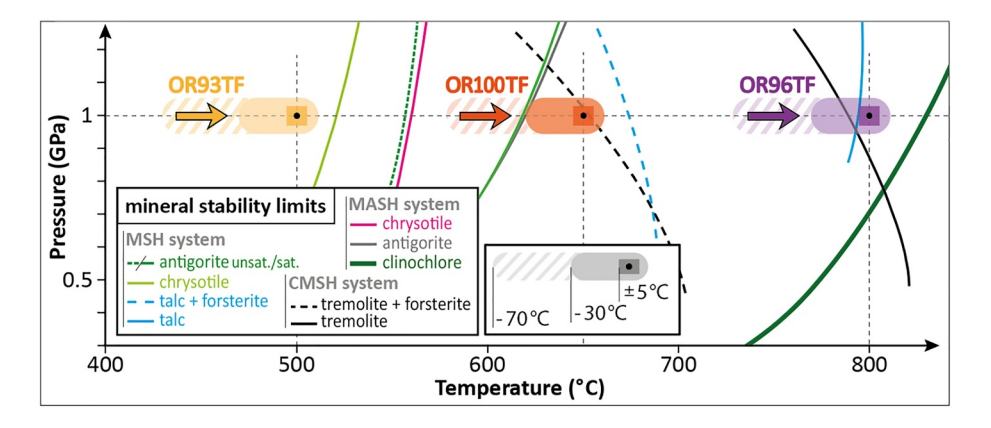


Figure 5. Pressure-Temperature diagram with the expected transformations during the runs. Experimental conditions are represented with yellow, red, and purple squares (temperature at thermocouple). Uncertainties on confining pressure and temperature are  $\leq 0.05$  GPa and  $\leq 5^{\circ}$ C. Shadows account for maximum variability radially (30°C) and vertically (70°C), as described in the text. The arrow shows the *P-T* path toward deformation conditions. The stability limit of clinochlore (major hydrous phase in the Åheim dunites), that is, MASH-system chlorite, is represented along with all minor phases identified in the starting material (except phlogopite, stable to higher temperatures).

FERRAND ET AL. 8 of 22

doi/10.1029/2025GC012629 by ESPCI ParisTech, Wiley Online Library on [26/11/2025]. See

Summary of the Experimental Ratio									
Run	Pressure	Temperature (°C)	Piston speed (mm s <sup>-1</sup> )	Mean sample strain rate (s <sup>-1</sup> )	Max. shortening (%)				
OR93TF	1 GPa	500	$1.0 \times 10^{-4}$	$7.1 \times 10^{-6}$	32.4				
OR96TF		800	$1.1 \times 10^{-4}$	$7.8 \times 10^{-6}$	36.7				
OR100TF		650	$8.0 \times 10^{-5}$	$3.2 \times 10^{-6}$	26.8				

of which might be significantly better based on previous experiments (Mansard et al., 2018), but this remains to be quantified. After the experiment, stress measurements must also be corrected from both the changing contact surface during sample widening and stiffness of the apparatus (Kido et al., 2016; Précigout et al., 2018). The latter was measured at 15 µm/kN using a tungsten carbide cylinder and a copper sleeve, respectively, in place of the sample column and confining medium, both compressed at 1 GPa (Figure S2 in Supporting Information S1). It should be noted that, due to the inner Ni electrode, the actual contact surface between the sample and piston is not equal to  $\pi \times r_{\rm ext}^2 \approx 50$  mm<sup>2</sup> but rather  $\pi \times (r_{\rm ext}^2 - r_{\rm in}^2) \approx 46$  mm<sup>2</sup>. However, as the assembly is confined by solid NaCl and considering that the downward extrusion of the electrode into the lower piston is limited, we can reasonably consider that it bears some part of the applied force. As a consequence, the value of the stress applied to the dunite sample should be comprised between  $\xi$  and  $\xi$ ?  $\approx 1.1 \times \xi$  respectively in plain and dashed black lines on Figure 6. The impact of Ni extrusion is illustrated in Figures 6, 7b, and 8, and discussed in Section 4.4.

#### 2.4. Microstructural Observations and Phase Identification

Following deformation experiments, samples were cut in half along the inner electrode, that is, vertically, and then prepared for characterization. Polished surfaces were investigated using light and scanning electron microscopy. Most of the observations were made using a *ZEISS Sigma* field emission scanning electron microscope. To determine the composition of either starting or deformed materials, we performed qualitative analyses using an *Oxford Instruments* Energy Dispersive Spectrometer. The chamber vacuum was  $2.50 \times 10^{-6}$  mbars, and the acceleration voltage was 15 kV. As the studied rocks are not electrically conductive at ambient temperature, the polished surfaces were coated with amorphous carbon for SEM imaging. Microstructural analyses on samples OR93TF, OR100TF, and OR96TF are respectively reported in Figures 9–11.

#### 3. Results

#### 3.1. Proof-of-Concept Experiment on Carrara Marble

To ensure the accuracy and reproducibility of the electrical data provided by the *ElectroGriggs* setup, we conducted a proof-of-concept experiment using Carrara marble, the mechanical and electrical results of which are provided in Figure 3. During the pumping stage of the experiment, which involves alternatively increasing pressure and temperature up to the first step of deformation conditions, the electrical conductivity remained around  $10^{-7}$  S m<sup>-1</sup>, with significant fluctuations during the building of the electrical circuit. Heating to  $500^{\circ}$ C led to a sharp increase in the conductivity. Deformation was launched at  $500^{\circ}$ C and 1 GPa by advancing the  $\sigma_1$  piston at a constant flow rate. The lead, on top of the assembly (Figures 1b and 2c), is first extruded until the hit-point is reached, that is, onset of sample deformation. Here, lead extrusion was characterized by relatively stable conductivity after initial stabilization. Elastic loading, starting around 22:30, was accompanied by a significant increase until we stopped the pump at 00:00, that is, peak stress after  $\approx 5\%$  shortening. The relaxation step gave rise to a sharp conductivity peak, followed by a quick drop that progressively evolved toward a gentle increase similar to the one observed during lead extrusion. In any case, conductivity values range between  $10^{-5}$  and  $10^{-6}$  S m<sup>-1</sup>, consistent with measurements for carbonates in static conditions (Mirwald, 1979; Ono & Mibe, 2015). This peak is due to the transient percolation of supercritical CO<sub>2</sub> (Mirwald, 1979).

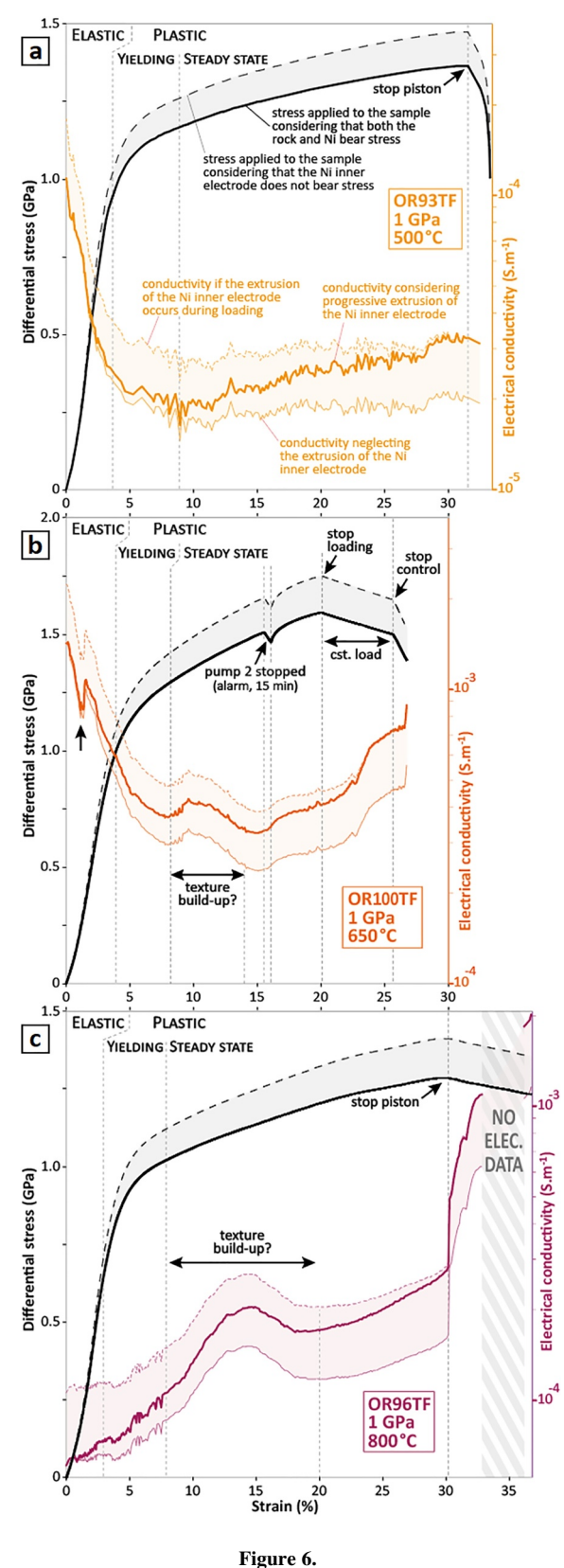
Following the first step of relaxation, we increased the temperature to 650°C, which instantaneously produced a sharp increase in conductivity until values within the range of available data from static experiments (Mirwald, 1979; Ono & Mibe, 2015). Re-starting the deformation pump simultaneously increased both the force and conductivity until we stopped the pump after 5% of finite strain. The conductivity then remained stable at around

FERRAND ET AL. 9 of 22

15252027, 2025, 11, Downlo

om/doi/10.1029/2025GC012629 by ESPCI ParisTech, Wiley Online Library on [26/11/2025]. See

Wiley Online Library for rules of use; OA articles are governed by the applicable Creative Commons Licens



rigure o.

 $10^{-4}$  S m<sup>-1</sup> all over mechanical relaxation, before increasing again at more than  $3.10^{-4}$  S m<sup>-1</sup> when we increased the temperature from 650 to 800°C. At such high temperatures, deformation did not produce any effect on conductivity, fixed around  $5.10^{-3}$  S m<sup>-1</sup>, near the range of conductivity values measured in static conditions for calcite and dolomite (Mirwald, 1979; Ono & Mibe, 2015).

During quenching, rather than dropping the temperature from 800 to 200°C in 2 min without pressure control, we left the confining pressure pump running to keep it constant at 1 GPa and stopped the quenching process at 650 and 500°C, leaving the conductivity stabilizing for a couple of minutes. These conductivity values are higher than the respective ones recorded during deformation (and relaxation), highlighting a direct effect of strain and/or high-temperature crystallization on electrical conductivity. Interestingly, a peak of conductivity was also observed at  $\approx\!350^\circ\text{C}$  and  $\approx\!0.9$  GPa during the final step of quenching from 500 to 200°C. Considering the phase diagram from CaCO<sub>3</sub> (Johannes & Puhan, 1971), this peak may occur due to cations re-arrangement during the transition from calcite to aragonite (Figure S3 in Supporting Information S1). The actual origin of this peak, along with the one observed during relaxation at 500°C, will be explored in future studies dedicated to the electrical conductivity of the Carrara marble.

### 3.2. Electrical Conductivity Versus Mechanical Data of the $\mathring{\mathbf{A}}$ heim Dunite

For the three sets of data presented here, the pressure transducers, load cell, displacement transducers, thermocouple and electrodes were functioning all along the experiments from pumping to quenching, so that we have a complete record of the pressure/stress, piston displacement and temperature, as well as a large and almost complete data set of sample electrical resistance. In Figures 6 and 7, we provide the mechanical data coeval with electrical conductivity from the starting point of sample deformation ("hit-point") to the time of quenching (not included). At 500°C (OR93TF), the electrical conductivity decreases during elastic loading from  $\approx 10^{-4}$  down to  $2 \times 10^{-5}$  S m<sup>-1</sup> (i.e., an order of magnitude) and tends to increase and fluctuate during plastic deformation (between  $2 \times 10^{-5}$  and  $3.3 \times 10^{-5}$  S m<sup>-1</sup>). In addition, short-period oscillations (3-4 datapoints, i.e., 11-14 min) of the conductivity values are noted in the plastic regime, far exceeding typical uncertainties. The latter is commented together with Microstructural observations in the Section 4. The electrical conductivity at 650°C (OR100TF) similarly decreased during loading from  $\approx$ 4 × 10<sup>-3</sup> down to 4 × 10<sup>-4</sup> S m<sup>-1</sup> (an order of magnitude) and then fluctuated between 4 × 10<sup>-4</sup> and 3 × 10<sup>-4</sup> S m<sup>-1</sup>. However, a sudden—but limited—

**Figure 6.** Evolution of the electrical conductivity and differential stress as a function of strain in the new-generation Griggs-type apparatus. (a) Experiment OR93TF performed on a Åheim dunite sample at a confining pressure of 1 GPa, a temperature of 500°C and an average strain rate of  $7.1 \times 10^{-6} \, \mathrm{s^{-1}} \, (\approx 1.0 \times 10^{-4} \, \mathrm{mm \, s^{-1}})$ . See text for definitions and error bars. (b) Experiment OR100TF performed on a Åheim dunite sample at a confining pressure of 1 GPa, a temperature of 650°C and a strain rate of  $3.2 \times 10^{-6} \, \mathrm{s^{-1}} \, (\approx 8 \times 10^{-5} \, \mathrm{mm \, s^{-1}})$ . The vertical arrow indicates a sudden increase in electrical conductivity during elastic loading while conductivity rather exhibits an overall decrease. The "texture build-up" refers to any textural or structural evolution that seems to affect the radial conductivity after sample yielding (onset of sample-scale plasticity). (c) Experiment OR96TF performed on a Åheim dunite sample at a confining pressure of 1 GPa, a temperature of 800°C and a strain rate of  $7.8 \times 10^{-6} \, \mathrm{s^{-1}} \, (\approx 1.1 \times 10^{-4} \, \mathrm{mm \, s^{-1}})$ .

FERRAND ET AL. 10 of 22

1525207, 2025, 11, Downloaded from https://agupubs.oninelibrary.wiely.com/doi/10.1029/2025GO12G9 by ESPCI ParisTech, Wiley Online Library on [26/11/2025]. See the Terms and Conditions (https://onlinelibrary.wiley.com/terms-and-conditions) on Wiley Online Library for rules of use; OA articles are governed by the applicable Creative Commons License

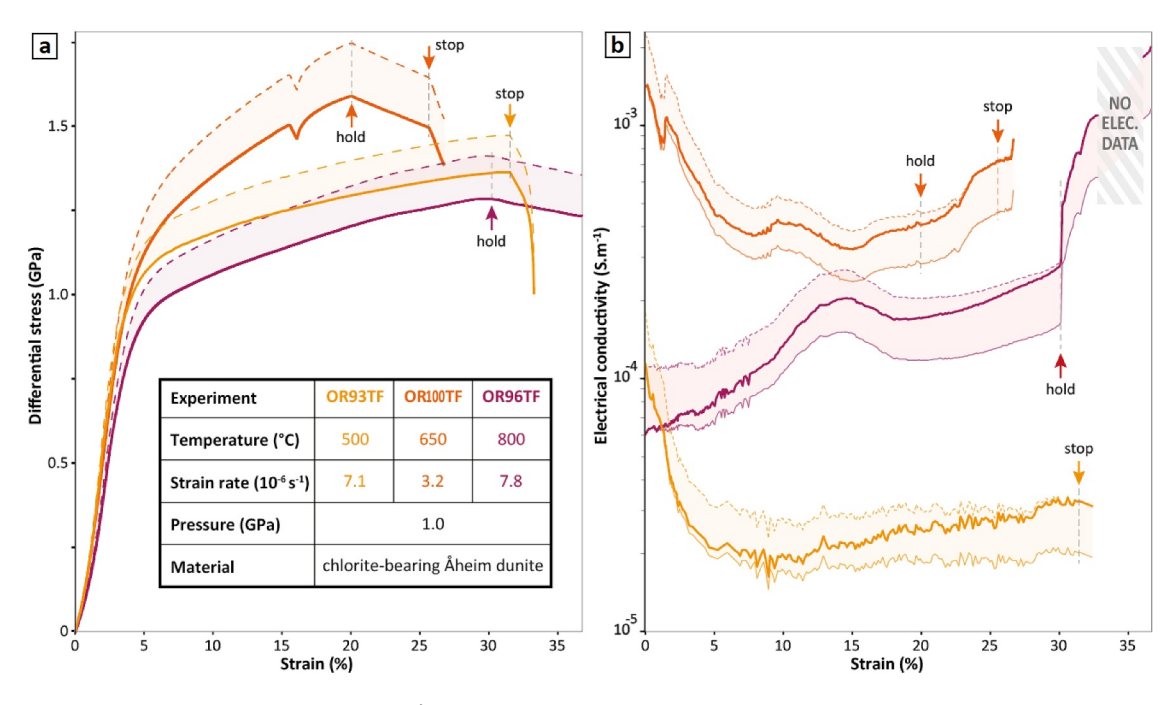


**Figure 7.** Direct comparison of the experimental results on the Åheim dunite deformed at 500, 650, and 800°C. (a) stress versus strain curves for the three experiments, with a recap of temperatures, strain rates, and pressure. (b) Electrical conductivity versus strain. The mark "hold" accounts for a switch from controlled strain to constant load, that is, the piston is stopped and the pumps keep controlling; "stop" indicates that there is no control to keep a constant load anymore. Details are provided in Figure 6.

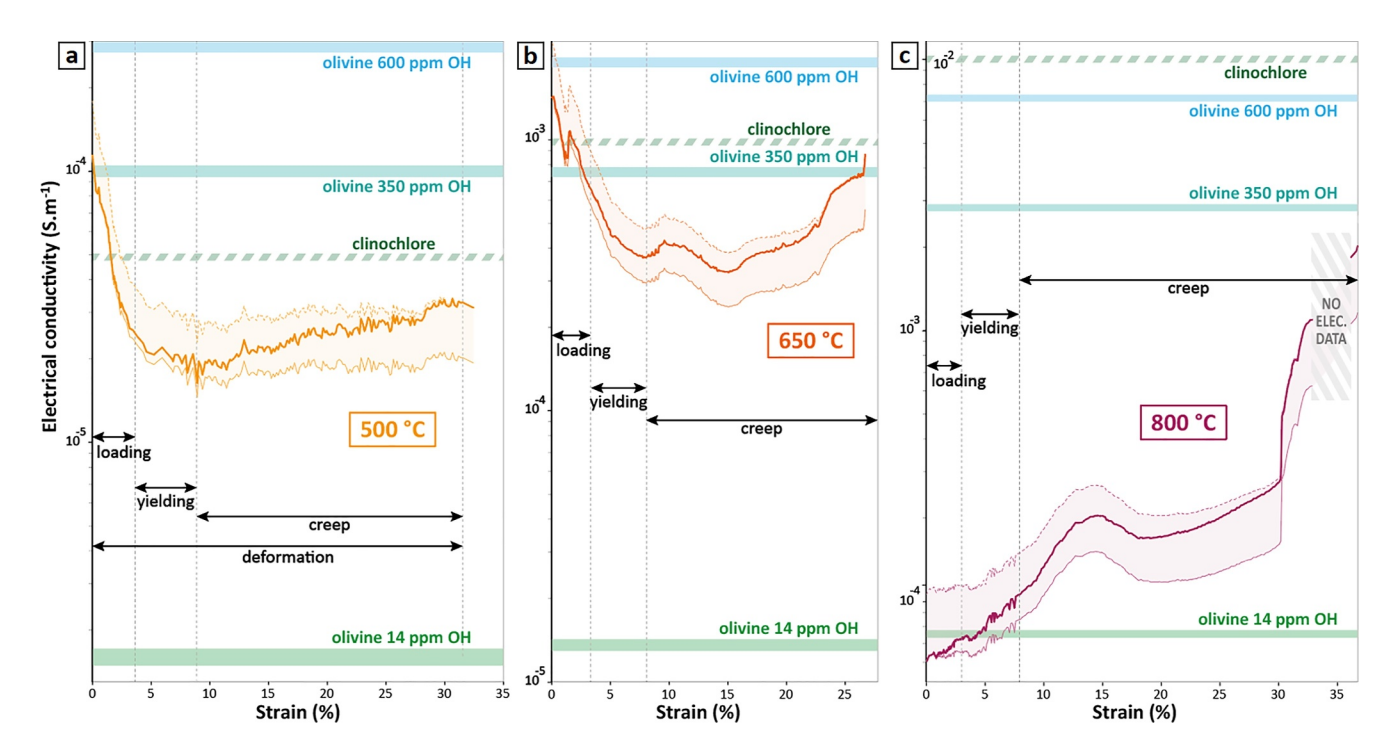


**Figure 8.** Results at 500°C (a), 650°C (b), and 800°C (c) compared to the typical conductivity of olivine with limited water content. Evolution of the conductivity with strain (Figures 6a–6c) compared to the typical conductivity of olivine with limited water contents of 14, 350, and 600 ppm (Gardés et al., 2014) and of clinochlore (Shen et al., 2023) for the same *P-T* conditions. The time window "loading" refers to initial elastic loading; "yielding" corresponds to the plastic transition, that is, elastic limit of the sample and onset of plasticity; "creep" refers to plastic strain. See mechanical data in Figures 6 and 7.

FERRAND ET AL. 11 of 22

15252027, 2025, 11, Downloaded from https://agupubs.onlinelibrary.wiley.com/doi/10.1029/2025GC012629 by ESPCI ParisTech, Wiley Online Library on [26/11/2025]. See the Term

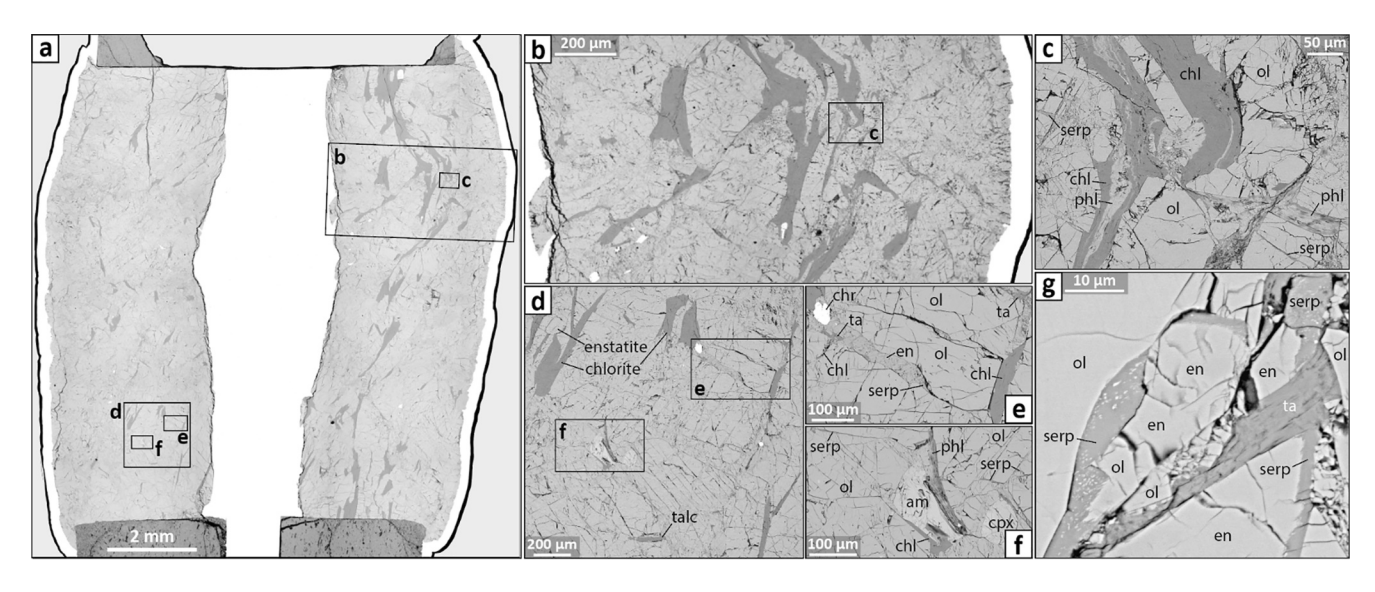


**Figure 9.** Microstructural observations on a subvertical section of sample OR93TF. Backscattered electron images and scanning electron microscopy. Run conditions: 1 GPa, 500°C. (a) full section showing the inner and outer electrodes (Ni and Ni + Pt, respectively) and the upper and lower pistons (alumina); (b) detailed view of a chlorite-rich region; (c) zoom with detailed mineralogy, revealing phlogopite stable with chlorite, as micrometric serpentine veins; (d–f) detailed view of a region with average chlorite content, showing the mineral diversity of the Åheim dunite, including talc, serpentine, phlogopite, and some calcic amphiboles; (g) typical micro-scale grain-boundary paragenesis between various hydrous phases, most of which consisting of talc and two serpentine minerals. Abbrev.: am = amphibole; chl = chlorite (clinochlore); chr = chromite; cpx = clinopyroxene; en = enstatite; ol = olivine (forsterite); phl = phlogopite; serp = serpentine (chrysotile and/or antigorite); ta = talc.

increase of conductivity (8  $\times$  10<sup>-4</sup> to 10<sup>-3</sup> S m<sup>-1</sup>) occurred within the loading phase (at  $\approx$ 1.4% strain; vertical arrow in Figure 6b), and a smoother transient increase was observed at the end of the yielding phase (at  $\approx$ 8% strain). This is followed by a similar, but permanent, increase of conductivity at  $\approx$ 16% strain when the deformation pump stopped due to a security alarm by applying a short relaxation step for 15 min. Finally, we applied a constant-load phase (i.e., oil pressure constant) between 20- and 26-% strain, which appeared characterized by a sigmoid increase of conductivity from  $\approx$ 4  $\times$  10<sup>-4</sup> to 7  $\times$  10<sup>-4</sup> S m<sup>-1</sup>.

In contrast, the sample deformed at 800°C (OR96TF; Figure 6c) did not exhibit any decrease in electrical conductivity, but rather a low initial conductivity value of  $6 \times 10^{-5}$  S m<sup>-1</sup>. Sample yielding is then characterized by a slight increase of conductivity to  $\approx 10^{-4}$  S m<sup>-1</sup>, with minor fluctuations. Importantly, from 8% strain, we observe a transient increase of conductivity reaching  $2 \times 10^{-4}$  S m<sup>-1</sup> at 14%–15% strain and back down to  $0.4 \times 10^{-4}$  S m<sup>-1</sup> at 20% strain, followed by further increase to  $\approx 2.8 \times 10^{-4}$  S m<sup>-1</sup> at 30% strain. Finally, switching to a constant load induces a strong increase in conductivity up to  $2 \times 10^{-3}$  S m<sup>-1</sup>.

#### 3.3. Microstructural Observations Versus Electrical Conductivity

In Figures 9–11, we provide microstructural observations of the three experiments on Åheim dunite. Overall, we first observe that the three dunite samples contain amounts of olivine ( $\approx$ 92 vol.%), chlorite ( $\approx$ 6 vol.%) and minor phases ( $\approx$ 2 vol.%) similar to the starting material (Figure 4). Chlorite (and minor phases) may appear somehow irregularly distributed at the sample scale (e.g., Figure 9a), which—as long as it remains stable—cannot have a major impact on bulk electrical conductivity because (a) chlorite conductivity is not much higher than that of the bulk (Figure 8), (b) zones with higher chlorite contents are only 2D views of volumes containing  $\approx$ 6 vol.% of chlorite between the inner and outer electrodes, and (c) chlorite crystals mostly exhibit a vertical shape preferred orientation when the conductivity is measured radially.

In the sample deformed at 500°C (OR93TF), diverse minor phases were identified with energy-dispersive X-ray spectroscopy, such as amphibole, chromite, pyroxenes, phlogopite, serpentine and talc (Figures 9c–9g). The relatively homogeneous sample-scale deformation is expressed by semi-brittle features at the microscale (e.g., Figure 9d). All mineral phases appear thermodynamically stable, but serpentinite is associated with minor iron

FERRAND ET AL. 12 of 22

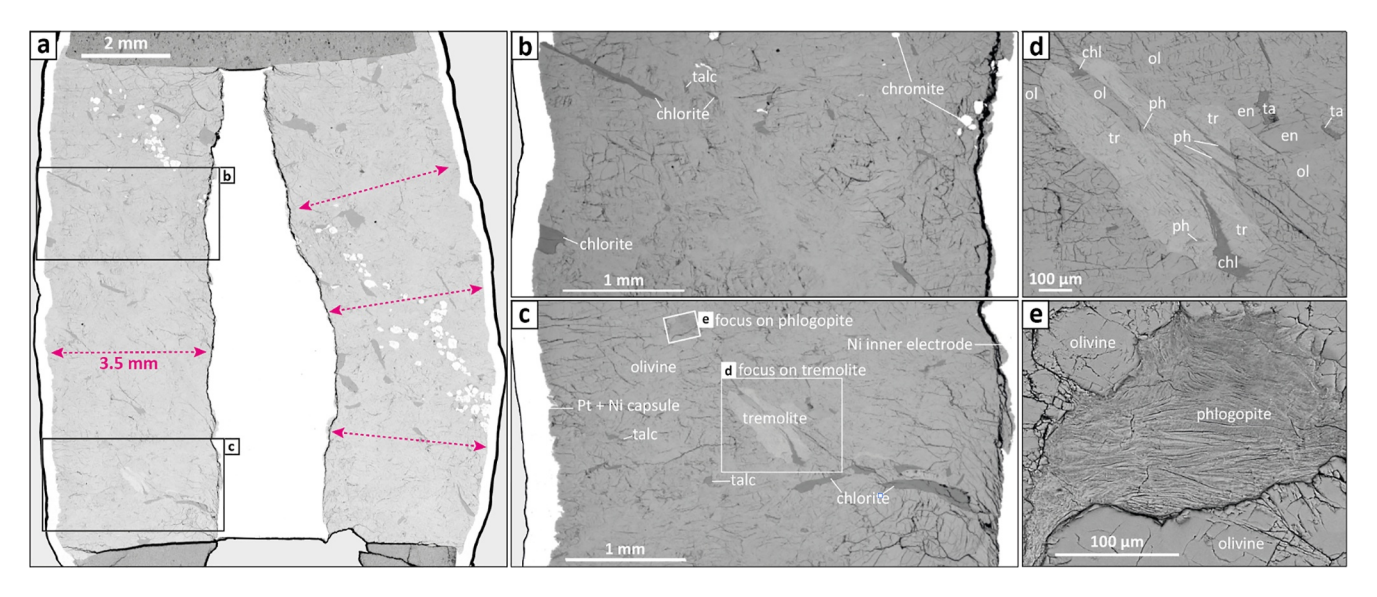


**Figure 10.** Microstructural observations on a subvertical section of sample OR100TF. Backscattered electron image and scanning electron microscopy. Run conditions: 1 GPa, 650°C. (a) full polished section; (b–c) focus on areas with representative mineralogy; (d) detailed view of a hydrous aggregate made of tremolite, chlorite, and phlogopite; (e) detailed view of a phlogopite. Pink arrows highlight low variability of rock thickness. Abbrev.: chl = chlorite (clinochlore); chr = chromite; en = enstatite; ol = olivine (forsterite); ph = phlogopite; ta = talc; tr = tremolite (amphibole); Pt = platinum; Ni = nickel.

oxide, whose alignment along serpentinite crystallographic planes would suggest minor chemical adjustment at elevated temperatures, releasing both iron and water (partial dehydration reactions; Ferrand, 2019b).

The sample deformed at 650°C (OR100TF) reveals the same mineral diversity (Figure 10), except for serpentinite, which was expected to breakdown (Figure 5) and has indeed dehydrated. Similar to the sample deformed at 500°C (OR93TF), the deformation was relatively homogeneous and no major structure developed at the sample scale (Figure 10a). Considering that the observed variations in electrical conductivity are solely controlled by temperature and water content (Figure 8), OR100TF seems a bit more hydrated than OR93TF at 500°C. The initial conductivity of OR100TF would indeed be consistent with a dunite containing 400–500 ppm  $H_2O$ , instead of 350 ppm for OR93TF (Gardés et al., 2014). This could result from the serpentinite breakdown that may release around 120 ppm of  $H_2O$  considering 0.1 vol.% of serpentinite (12% × 0.1%  $\approx$  0.012% = 120 ppm). Finally, we note some over-representation of chromite in sample OR100TF (polished surface; Figure 10a). Chromite is highly conductive ( $\approx$ 1 S m<sup>-1</sup> at 650°C), leading to bulk conductivities of  $\approx$ 2.5 × 10<sup>-4</sup> S m<sup>-1</sup> in olivine aggregates with 4% connected chromite (instead of 3.2 × 10<sup>-5</sup> S m<sup>-1</sup>; Sun et al., 2021). Nonetheless, the Åheim dunite contains <<1% disconnected chromite, so we can neglect its influence in this study.

Detailed microstructural observations show (semi)brittle features in all three samples, but only deformation at 800°C (OR96TF) has localized strain in the form of macroscopic faulting (Figure 11). The polished section reveals a fault segment going through a highly deformed aggregate of talc and olivine, that is, products of serpentine breakdown (Berman et al., 1986); instead, full clinochlore dehydration (breakdown) would have produced aggregates of olivine, enstatite and spinel (Staudigel & Schreyer, 1977), not observed in this study. At 800°C, serpentinite is expected to undergo fast dehydration due to the overshoot of its stability limit. A ductile-to-brittle transition was reported at the sample scale in serpentinites at high temperatures (e.g., Proctor & Hirth, 2016) and would be the mechanical signature of minor mineral transformation locally at the microscale (Ferrand, 2019a). The embrittlement of the Åheim dunite (macroscopic faulting) reported under these conditions, compared to homogeneous sample-scale deformation at 500 and 650°C (OR93TF and OR100TF), likely originates from a catastrophic stress transfer due to local dehydration of minor amounts of hydrous minerals (e.g., Figure 11d), for example, serpentine (Ferrand et al., 2017).

FERRAND ET AL. 13 of 22

15252027, 2025, 11, Downloaded from https://agupubs.onlinelibrary.wiley.com/doi/10.1029/2025GC012629 by ESPCI ParisTech, Wiley Online Library on [26/11/2025]. See the Term

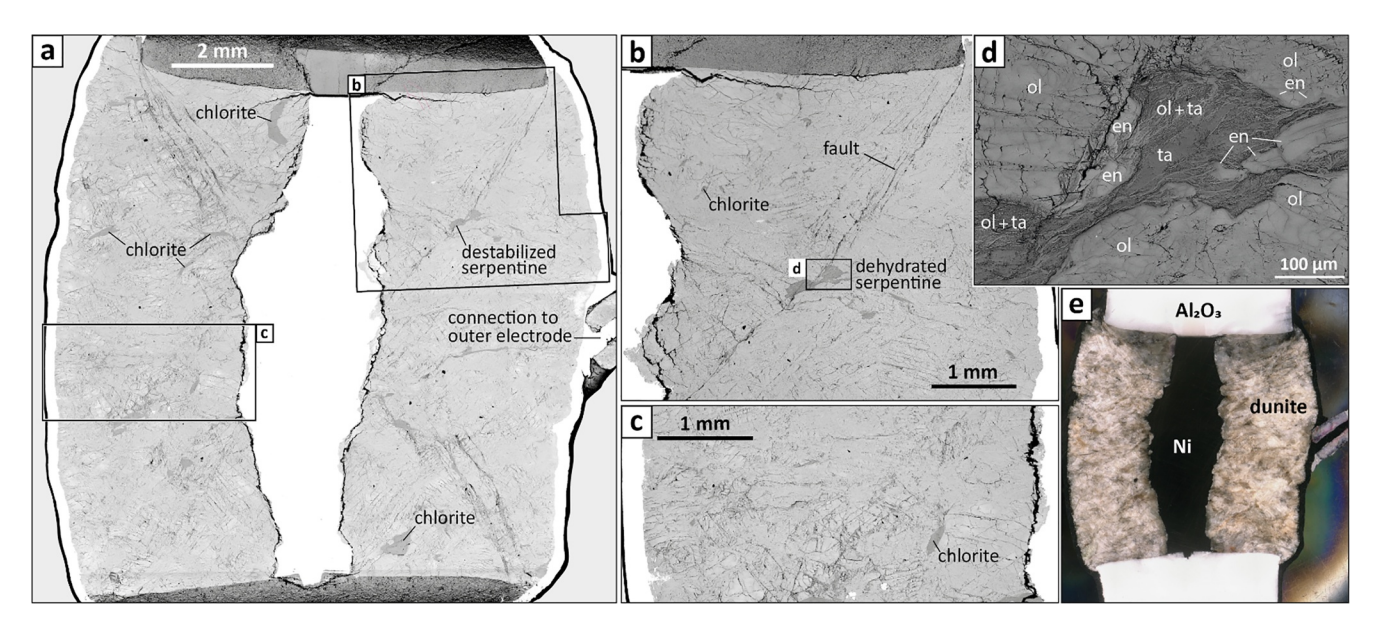


**Figure 11.** Microstructural observations on a subvertical section of sample OR96TF. Backscattered electron image and scanning electron microscopy. Run conditions: 1 GPa, 800°C. Pink arrows highlight low variability of rock thickness. (a) full polished section; (b) macroscopic fault connected to dehydrated serpentine; (c) detailed view of an area characterized by semi-brittle deformation; (d) detailed view of a dehydrated serpentine cluster; (e) light microscopy image. Abbreviations: chl = chlorite (clinochlore); en = enstatite; ol = olivine (forsterite); ph = phlogopite; ta = talc; tr = tremolite (amphibole).

#### 4. Discussion

#### 4.1. Grain Boundaries and the Role of H<sub>2</sub>O

In olivine aggregates, as in most silicates, grain boundaries constitute high diffusivity pathways and are the main carriers of electrical charges (e.g., Fisher, 1951; Fisler et al., 1997; Mantisi et al., 2017; Marquardt & Faul, 2018). Grain boundary diffusivity can be orders of magnitude higher than that of crystals (e.g., Demouchy, 2010; Novella et al., 2017). These high-diffusivity pathways can have variable geometries, which can be approximated by several simple models (e.g., Ferrand, 2020). In addition, most water defects (or free water, if any) are distributed at grain boundaries (e.g., Ferrand & Chin, 2023; Hiraga et al., 2004; Précigout et al., 2019; Sommer et al., 2008), which significantly increases electrical conductivity notably via networks of hydrogen bonds either at grain boundaries or as crystal defects (e.g., Karato, 1990; Yoshino, 2010).

In our case, electrical conductivity is measured radially (horizontally) between the inner and outer electrodes during a vertical mechanical loading. On Carrara marble, we describe an increase in conductivity with increasing strain at 500 and 650°C, particularly revealed during the quenching stage. This feature is consistent with the effect of grain boundaries that flatten and parallelize into the plane normal to the shortening axis. However, for OR93TF (500°C) and OR100TF (650°C) on Aheim dunite, the conductivity first gradually decreases down to an order of magnitude during mechanical loading in the elastic regime (Figures 6a and 6b). As the yield stress is not reached, no additional grain boundaries (crack) are formed, and thus the only way to decrease radial electrical conductivity is to reduce the volume of conductive materials, which for dunites can only be done by thinning grain boundaries. Therefore, we interpret the reduced electrical conductivity with increasing axial stress as due to thinning of the grain boundaries oriented (sub)horizontally (i.e., normal to the compression axis). Following the yield stress, that is, in the plastic regime, grain boundaries are then expected to be progressively transposed into the plane normal to the maximum stress during deformation, giving rise to a progressive increase of conductivity, as documented for all our experiments. However, the experiment OR96TF (800°C; Figure 6c) does not record any drop in conductivity before plastic yielding (<3% strain, i.e. elastic domain), but rather an initially low conductivity (≤10<sup>-4</sup> S m<sup>-1</sup>). Such a low electrical conductivity indicates that grain boundaries did not contain much water (Gardés et al., 2014). Thus, contrary to what is observed at lower temperatures, at 800°C, full dehydration of grain boundaries occurs before deformation. This temperature is high enough for all serpentinite to dehydrate and, as the capsule is open (Pt tube around direct contacts between dunite and alumina; Figure 2), release most free H<sub>2</sub>O outside of the sample.

FERRAND ET AL. 14 of 22

The fact that the capsule is open allows free water produced by potential dehydration reactions within the samples to escape the system, for instance upon sample-scale percolation. The relatively high conductivity values recorded at 500 and 650°C are consistent with the expected values for olivine polycrystals (Gardés et al., 2014; Figure 8) with minor fluid production due to the dehydration of serpentine ("serp", still stable in sample OR93TF, 500°C), which we estimate to be around 0.1 vol.% from SEM imaging (Figure 9). With serpentine containing  $\approx 12\% \ H_2O$ , the expected amount of free water produced upon its dehydration is  $12\% \times 0.1\% \approx 0.012\% = 120$  ppm, which could well explain the difference in starting conductivity between OR93TF (500°C; 350 ppm  $H_2O$ ) and OR100TF (650°C; 400–500 ppm  $H_2O$ ). These electrical conductivity values are consistent with the expected values for well-preserved dunites with  $\approx 350$ –600 ppm  $H_2O$  (Gardés et al., 2014). At 1 GPa, serpentinite minerals are supposed to be fully dehydrated above 560°C (chrysotile) and 625°C (antigorite), as expected from thermodynamics (pink and gray curves in Figure 5). As serpentinite is not found in OR100TF (650°C; Figure 10), we interpret that serpentinite destabilized within the dunite before deformation. Dehydration-induced water would have wetted grain boundaries (Précigout et al., 2017, 2019), thus increasing the conductivity of these high-diffusivity pathways (Gardés et al., 2014; Marquardt & Faul, 2018).

Clinochlore conductivity at 500, 650, and 800°C is also reported in Figure 8, with values of  $1.6 \times 10^{-4}$ ,  $1.1 \times 10^{-3}$ , and  $10^{-2}$  S m<sup>-1</sup>, respectively (1 GPa; Shen et al., 2023). Interestingly, the electrical conductivity of stable clinochlore (12 wt.% H<sub>2</sub>O) is close to that of a dunite that would contain 300–400 ppm H<sub>2</sub>O. In addition, in this study clinochlore is only 5–7 vol.% and is not radially connected. Consequently, as long as it is stable, it can be neglected when interpreting conductivity changes. In such hydrous minerals, protons are part of the lattice, whereas in olivine aggregates, protons form a network of OH bonds at grain boundaries (so-called "water defects") that eventually enhance the conductivity of these high-diffusivity pathways (Ferrand & Chin, 2023; Fisher, 1951). At 1 GPa, clinochlore is expected to remain thermodynamically stable up to  $\approx$ 815°C (Figure 5). This is confirmed for runs OR93TF (500°C; Figure 9) and OR100TF (650°C; Figure 10), but chlorite shows signs of instability at 800°C (run OR96TF; Figure 11) due to proximity with its breakdown conditions (Figure 5), which might contribute to the transient/overall increase of conductivity during deformation at 800°C.

The low conductivity recorded at  $800^{\circ}$ C reveals that the sample has been dried (free water has escaped the system; Figure 8c) before the onset of controlled deformation. In other words, serpentine has already been fully consumed and water either consumed by newly formed minerals (talc; Figure 11d) and/or dried out via assembly scale percolation. The final increase of conductivity upon relaxation (up to  $\approx 10^{-3}$  S m<sup>-1</sup> only) would rather be consistent with limited horizontal percolation of fluids coming from partial/local destabilization of chlorite. It must be clarified that the link between electrical conductivity changes and water production (mineral reaction) is not straightforward as electrical conductivity would rather be mainly controlled by the establishment of fluid percolation networks.

Changes in radial conductivity appear directly due to axial compression, as mechanical stress favors vertical grain-boundary fluid percolation upon loading (Figures 6a and 6b; <3% strain) and horizontal fluid percolation upon unloading or relaxation (Figure 6c; >30% strain). This significant and direct impact on electrical conductivity at the sample scale likely results from the modulation of the thickness and geometry of grain boundaries, which intrinsic conductivity is expected stable at fixed pressure, temperature and water content. We observe conductivity changes ranging about one order of magnitude over 6%–7% strain for 5–6 hr. Since the conductive phase is already connected, this is not a topological change, but rather an increase in its volume fraction. Assuming that grain-boundary compressibility is the sole cause of conductivity changes in the elastic regime, and assuming a transversely isotropic medium, the surface fraction of grain boundaries would have changed over an order of magnitude, that is, multiplied by 10 to explain the increase of effective conductivity by 10. However, the thickness of grain boundaries can only be pinched by 10%–50% (Hansen et al., 2012; Thieme et al., 2023; Wheeler et al., 2001). Thus, the presence of (free) volatiles at grain boundaries in the dunite must contribute to the observed conductivity variations by densifying the distribution of OH bonds that favor electron mobility. Either OH re-arrangement or stress-induced fluid percolation events are likely at grain boundaries to explain the observed electrical conductivity values.

#### 4.2. Deformation as a First-Order Parameter to Control Electrical Conductivity

In our experiments, we confirm that temperature has a strong effect on electrical conductivity, but we also demonstrate how the latter may significantly change over strain, either elastic (linearly related to stress) or plastic

FERRAND ET AL. 15 of 22

(denser conductive networks due to fracturing), especially if mobile defects (e.g., water) are present at grain boundaries. Although not observed for Carrara marble—probably because calcite is much weaker than olivine this is particularly the case at 500 and 650°C for Aheim dunite, where the conductivity first decreases during elastic loading, and then increases with plastic strain. How the sample deforms (elastic vs. plastic) thus strongly influences the electrical conductivity, here attributed to closing, and then transposition of H<sub>2</sub>O-rich grain boundaries. Furthermore, in contrast to the experiment at 500°C, deformation at both 650 and 800°C involves an onset of plasticity associated with a transient increase in electrical conductivity. Based on microstructural observations (e.g., Figure 9d), this feature would result from fracturing or faulting events that produce electrical pathways by-passing the tortuosity of grain boundaries and allowing sample-scale percolation of dehydrationinduced fluids. A larger signature was observed at 800°C, for which major faulting occurred during deformation (Figures 11a and 11b). The sample-scale, cross-like geometrical distribution of these macroscopic faults also indicates that stress plays a major role in their production; they nucleate and develop from stress concentrations (e.g., edges of the top piston; Figure 11b). Moreover, considering conductivities of  $10^{-4}$  and  $4 \times 10^{-3}$  S m<sup>-1</sup> respectively measured at 500 and 650°C, and being aware that electrical conductivity increases with increasing temperature, we would have expected a conductivity >10<sup>-2</sup> S m<sup>-1</sup> at 800°C, assuming that clinochlore remains fully stable and that the system can be considered closed. This feature is consistent with a deformed material that has undergone a physical change, the effect of which involves a sharp increase in conductivity when the deformation is stopped. Further experimental investigations are required to understand the exact nature of these

The short-period fluctuations observed during plastic deformation of Åheim dunite at 500°C are more difficult to interpret. As explained before, they do not consist of systematic ups and downs from one measurement to another, and their amplitude is larger than what we expect from uncertainties on resistance estimates (Figure S1 in Supporting Information S1). Short-period fluctuations are possibly the signature of transient processes occurring at the microscale within the sample or may be due to either small-scale fluid percolation events resulting from local dehydration of serpentinite or semi-brittle events. Faulting, grain crushing, and fluid percolation can be closely related. Further investigations would be required, including a series of additional experiments, to understand what it is about.

In any case, these results strongly suggest that deformation (especially elastic strain) may strongly modulate fluid-dominated electrical anomalies. Stress and strain have indeed a significant impact on electrical conductivity by controlling the shape and number of electrically conductive features, which consist of faults and fractures at the sample scale, and grain boundaries at the microscale. Although our data set here remains preliminary/limited, we thus urge geoscience researchers to consider deformation as an important factor when proposing interpretations of electrical conductivity profiles, especially magnetotelluric (MT) profiles that can image deeper than 30 km ( $\approx$ 1 GPa).

#### 4.3. Geophysical Implications and Perspectives

To date, more than 99% of HP-HT electrical conductivity data come from laboratory experiments that do not consider the effect of deviatoric stress and deformation processes (e.g., Dai & Karato, 2009; Dai et al., 2012; Gaillard, 2004; Gardés et al., 2014; Karato, 2006; Sifré et al., 2014). However, many natural anomalies of electrical conductivity (MT profiles for large scales) characterize rocks that are currently experiencing significant deformation, which appear to be often correlated with moderate to high anisotropy (Kluge et al., 2022; Lemonnier et al., 1999; Masana et al., 2004; Unsworth et al., 2005). We demonstrate that stress and strain can significantly modulate electrical conductivity values, bringing in light that MT studies, especially revealing deep (>20 km depth) high-conductivity anomalies, are far from finding a simple explanation. As measuring *in situ* electrical conductivity during deformation of a significantly large sample, the *ElectroGriggs* thus opens a new era in experimental geophysics, with implications including either the interpretations of electrically conductive anomalies in MT models (e.g., Ingham & Brown, 1998; Naif et al., 2013) or earthquake physics (e.g., Ferrand et al., 2021).

Active fault zones exhibit various electrical signatures, the interpretation of which requires experimental data sets on known/simplified systems (e.g., Fazzito et al., 2009; Mazzella & Morrison, 1974; Ritter et al., 2005; Zhu et al., 2009). MT profiles in tectonically active regions have revealed electrical anomalies in various depth ranges (e.g., Ingham & Brown, 1998; Jiracek et al., 2007; Türkoğlu et al., 2008; Unsworth, 2010; Unsworth et al., 2005;

FERRAND ET AL. 16 of 22

Xu et al., 2019). The North and East Anatolian Faults provide very variable electrical conductivity profiles along strike (e.g., Karaş et al., 2017, 2020; Kaya et al., 2013; Türkoğlu et al., 2015); the Alpine Fault, accommodating most of the relative movement between the Pacific and Australian plates in New Zealand, is characterized by a deep (>8 km) electrical conductivity anomaly (10<sup>-1</sup>–1 S m<sup>-1</sup>) in its aseismic (ductile) part. The latter coincides with a low seismic velocity, so it is assumed to result from a network of electrolytic fluids, rather than partial melting or connected solid phases (Kluge et al., 2022). Conversely, the Alhama de Murcia Fault (SE Spain; e.g. Masana et al., 2004) is associated with a strong electrical conductivity anomaly (1–10 S m<sup>-1</sup>) between 0.4 and 1 km below the surface (fragile domain), interpreted by the circulation of fluids in fractured rocks (Martí et al., 2020). Although non-trivial, these profiles show links between electrical anomalies and large-scale strain localization, but without providing any simple/direct explanation.

In Nepal, a conductive anomaly ( $\approx 0.1 \text{ S m}^{-1}$ ) at 15–30 km depth (Lemonnier et al., 1999) seems to be associated with strong seismicity (Adhikari et al., 2021). Studies have questioned their lateral extension and sustainability (e.g., Unsworth, 2010). In southern Tibet, high conductivities would be due to hydrothermal fluids or partial melting (e.g., Li et al., 2003), recalling the great uncertainties regarding compositions and thermal regimes at these depths. While high conductivities linked to the thermal regime would be expected to be regional and stable (Unsworth et al., 2005), those due to the percolation of hydrothermal fluids are likely to fluctuate (Girault et al., 2018, 2023). In Nepal, large-scale structural irregularities are suspected to favor fluid percolation, whose links with seismicity (Adhikari et al., 2021) must be explored. We thus encourage further developments integrating both electrical and acoustic monitoring to better understand deep fault zones. While acoustic emissions tell us about strain localization and seismicity (e.g., Ferrand et al., 2017; Gasc et al., 2022), active acoustics provide information about seismic velocities, reduced by the presence of fluids (Moarefvand et al., 2021), and electrical conductivity can inform about the connectivity of these fluids and thus their ability to percolate (e.g., Laumonier et al., 2017; Martí et al., 2020). Furthermore, the design proposed in this study could even bring new insights regarding the nature of the transient low-viscosity material that lubricates dynamic sliding and facilitates the propagation of the seismic rupture (Ferrand et al., 2021).

Coeval changes in the seismic and electrical properties of faults have been widely observed in sub-surface conditions (e.g., Eberhart-Phillips et al., 1995) and laboratory analogs (Glover et al., 1996; Jouniaux et al., 2006). Seismic processes are known to induce modifications in the electrical field (Fujinawa et al., 2011). The conductivity peaks we observed (Figure 6a) might indicate microfaulting with a much higher sensibility than what we can see from sample-scale mechanical data. In the case of dynamic propagation, interpretations should also consider the suction effect in the dilatant quadrant that can either affect the dynamic lubricant (Ferrand et al., 2018) or pre-existing pore fluids (e.g., Brantut, 2020), as suspected along deep segments of the San Andreas Fault (Mazzella & Morrison, 1974).

Existing data sets only allow separate discussions about stress and electrical conductivity (e.g., Karato, 2006; Pommier et al., 2018), which cannot address in situ processes affecting for example, the state of matter in cracks or grain boundaries with increasing stress. As mentioned in the introduction, only a few high-pressure deformation experiments (≥0.7 GPa) could be performed using coeval stress and electrical conductivity measurements. Previous experimental series reported shear-parallel conductivity values one order of magnitude higher than those normal to shear (e.g., Zhang et al., 2014) already suggested that stress and strain cannot be ignored in the interpretation of electrical anomalies in fault zones. Unfortunately, the experimental design only allowed shear experiments on thin gouges, which can contribute to understanding fault zones with variable thicknesses or degrees of maturity, but are unable to address strain localization processes involved in faulting. In contrast, the *ElectroGriggs* allows pure shear deformation on centimetric cylinders (15 mm high, 8 mm thick), which can be used to study strain localization processes associated with earthquake triggering within intact samples.

The LAB is another example of strain localization feature locally associated with electrically conductive anomalies. Generally considered as a rheological limit between the rigid lithosphere and the convective asthenosphere, the LAB may contain melt or volatiles (D. H. Green et al., 2010; Hirth & Kohlstedt, 1996; Rychert et al., 2020; Schmerr, 2012). High electrical conductivity is reported at the LAB in the spreading direction  $(8 \times 10^{-2} \text{ S m}^{-1})$  compared to the ridge direction  $(3 \times 10^{-3} \text{ S m}^{-1};$  Evans et al., 2005; Baba et al., 2006). Such values and contrasts could be explained by the presence of a small melt fraction in the spreading direction (Caricchi et al., 2011; Naif et al., 2013; Yoshino et al., 2010). This has become, along with fluids, the basis for interpretations about the nature of the LAB in numerous studies (e.g., Kawakatsu et al., 2009; Naif et al., 2013;

FERRAND ET AL. 17 of 22

loi/10.1029/2025GC012629 by ESPCI ParisTech,

Stern et al., 2015). However, interrogations have recently emerged from lab experiments (e.g., Ferrand & Deldicque, 2021; Yamauchi & Takei, 2020), highlighting other parameters capable of significantly slowing down seismic waves or increasing conductivity, such as a small grain size, that is, high density of grain boundaries (charge carriers; Ten Grotenhuis et al., 2004), or the presence of volatiles that increase grain-boundary diffusion (e.g., Karato, 1990). The link between conductive anomalies and the potential presence of melt-rich channels has further been questioned by recent experimental results (Ferrand & Chin, 2023) and could rather be explained by the presence of garnet pyroxenite (fossilized LAB; Ferrand, 2020). The *ElectroGriggs* can reproduce strain localization at P-T conditions relevant for the LAB (i.e., P = 2–4 GPa and T > 1,000°C) and shows that deformation at such depth can increase the electrical conductivity by producing electrically conductive pathways, either transient or sustainable. Thus, the anisotropic nature of electrically conductive anomalies at the LAB would not necessarily be (fully) compositional.

#### 4.4. Further Improvements and Technical Developments

Uncertainties can arise from the resistance measurement, but they remain limited (e.g.,  $100 \Omega$  error bar for  $R = 2 k\Omega$  and  $400 \Omega$  for  $R = 7 k\Omega$ ; Figure S1 in Supporting Information S1), which leads to maximum errors about the size of datapoints on Figure 6. Therefore, in the calculation of the conductivity from the resistance, it is important to consider any factor that could influence the distance between the inner Ni electrode and the outer Ni sleeve, and the surface between the sample and electrodes. The sample surface is assumed constant during deformation considering that shrinking is fully accommodated by inner deformation of the Ni electrode. Sample height is easily estimated as we impose strain and can precisely measure it (Précigout et al., 2018), but it is important to notice that some Ni can be extruded downwards inside the hole of the lower piston (e.g., Figure 9a), therefore reducing the contact surface between the sample and the electrode. This defect in our setup results in a slight underestimate of the conductivity and uncertainties due to the unknown dynamics of Ni extrusion. The impact of the latter is reported in Figure 6 and will vanish with further developments. In addition, we note that the distance between the inner and outer electrodes, although it increases with axial shrinking, remains relatively homogeneous from top to bottom, as confirmed by SEM observations (e.g., pink arrows in Figure 10).

Finally, experimental conductivity measurements at high P and T are subject to the risk of shortcuts or disconnections of the electrical circuits (e.g., Pt wire broken under pressure due to asymmetry/defects in the assembly). Usually, thermocouples and electrodes become efficient after initial compression and/or heating. Under high P-T conditions, defects in the assembly may also prevent electrical current to pass through the rock sample. Out of the four experiments on dunite, only one (OR99TF) failed to provide electrical conductivity measurements. The origin of the problem remains unknown as surprisingly the electrodes remained connected even after unloading.

#### 5. Conclusions

We report the first measurements of rock electrical conductivity during experimental deformation of Carrara marble—as a proof-of-concept experiment—and Aheim dunite samples in a new-generation Griggs-type apparatus at a pressure of 1 GPa and temperatures of 500, 650, and 800°C. Upon adaptation of the sample assembly to perform synkinematic electrical conductivity measurements, we show that deformation strongly impacts the electrical conductivity of rocks, including olivine-rich rocks containing substantial amounts of water in either chlorite, minor hydrous phases, or grain boundaries. At 500 and 650°C, the radial electrical conductivity of dunite (normal to maximum compressive stress) drops down to an order of magnitude during mechanical loading. This is interpreted by squeezing grain boundaries that are oriented normal to the compressive deviatoric stress. In contrast, at 800°C, the dunite sample only records an increase in conductivity until we quench the sample; no drop in conductivity is observed during elastic loading, probably because grain boundaries have been dried during the pumping stage. Furthermore, at 650 and 800°C, the onset of plasticity is associated with a transient increase in electrical conductivity, interpreted as the emergence and development of faulting events based on microstructural observations. Plasticity would form new-grain boundaries and allow relaxation of other grain boundaries, leading to an increase of electrical conductivity. The data presented here are the first of a brand-new experimental data set, opening the scope of experimental geophysics for significant achievements to come, including valuable contributions to reducing the interpretive non-uniqueness of geophysical signatures.

FERRAND ET AL. 18 of 22

15252027, 2025, 11, Downloaded from https://agupub

nlinelibrary.wiley.com/doi/10.1029/2025GC012629 by ESPCI ParisTech,

ibrary on [26/11/2025]. See

#### **Conflict of Interest**

The authors declare no conflicts of interest relevant to this study. Open Access funding enabled and organized by Projekt DEAL.

#### **Data Availability Statement**

All electrical and mechanical data are available via Ferrand and Précigout (2025).

#### Acknowledgments

We thank the Alexander von Humboldt Foundation (Germany) and the Labex VOLTAIRE (ISTO, Université d'Orléans, France) for funding this research. T.P.F. acknowledges Damien Deldicque (LG-ENS) for the help with microstructural investigations. Open Access funding enabled and organized by Projekt DEAL.

#### References

- Adhikari, L. B., Bollinger, L., Vergne, J., Lambotte, S., Chanard, K., Laporte, M., et al. (2021). Orogenic collapse and stress adjustments revealed by an intense seismic swarm following the 2015 Gorkha earthquake in Nepal. Frontiers in Earth Science, 9, 659937. https://doi.org/10.3389/feart.2021.659937
- Baba, K., Chave, A. D., Evans, R. L., Hirth, G., & Mackie, R. L. (2006). Mantle dynamics beneath the East Pacific Rise at 17 S: Insights from the Mantle Electromagnetic and Tomography (MELT) experiment. *Journal of Geophysical Research: Solid Earth*, 111(B2). https://doi.org/10.1029/2004jb003598
- Barnhoorn, A., Bystricky, M., Burlini, L., & Kunze, K. (2004). The role of recrystallisation on the deformation behaviour of calcite rocks: Large strain torsion experiments on Carrara marble. *Journal of Structural Geology*, 26(5), 885–903. https://doi.org/10.1016/j.jsg.2003.11.024
- Berckhemer, H., Kampfmann, W., Aulbach, E., & Schmeling, H. (1982). Shear modulus and Q of forsterite and dunite near partial melting from forced-oscillation experiments. *Physics of the Earth and Planetary Interiors*, 29(1), 30–41. https://doi.org/10.1016/0031-9201(82)90135-2
- Berman, R. G., Engi, M., Greenwood, H. J., & Brown, T. H. (1986). Derivation of internally consistent thermodynamic data by the technique of mathematical programming: A review with application the system MgO-SiO<sub>2</sub>-H<sub>2</sub>O. *Journal of Petrology*, 27(6), 1331–1364. https://doi.org/10.1093/petrology/27.6.1331
- Bertrand, E. A., Caldwell, T. G., Hill, G. J., Bennie, S. L., & Soengkono, S. (2013). Magnetotelluric imaging of the Ohaaki geothermal system, New Zealand: Implications for locating basement permeability. *Journal of Volcanology and Geothermal Research*, 268, 36–45. https://doi.org/10.1016/j.jvolgeores.2013.10.010
- Börner, J. H., Girault, F., Bhattarai, M., Adhikari, L. B., Deldicque, D., Perrier, F., & Spitzer, K. (2018). Anomalous complex electrical conductivity of a graphitic black schist from the Himalayas of central Nepal. *Geophysical Research Letters*, 45(9), 3984–3993. https://doi.org/10.1029/2018s1077178
- Brantut, N. (2020). Dilatancy-induced fluid pressure drop during dynamic rupture: Direct experimental evidence and consequences for earthquake dynamics. Earth and Planetary Science Letters, 538, 116179. https://doi.org/10.1016/j.epsl.2020.116179
- Bruijn, R. H., Kunze, K., Mainprice, D., & Burlini, L. (2011). Mechanical and microstructural development of Carrara marble with pre-existing strain variation. *Tectonophysics*, 503(1–2), 75–91. https://doi.org/10.1016/j.tecto.2010.09.029
- Burnley, P. C., & Green, H. W. I. I. (1989). Stress dependence of the mechanism of the olivine–spinel transformation. *Nature*, 338(6218), 753–756. https://doi.org/10.1038/338753a0
- Caricchi, L., Gaillard, F., Mecklenburgh, J., & Le Trong, E. (2011). Experimental determination of electrical conductivity during deformation of melt-bearing olivine aggregates: Implications for electrical anisotropy in the oceanic low velocity zone. Earth and Planetary Science Letters, 302(1–2), 81–94. https://doi.org/10.1016/j.epsl.2010.11.041
- Chopra, P. N., & Paterson, A. M. (1981). The experimental deformation of dunite. Tectonophysics, 78(1-4), 453-473. https://doi.org/10.1016/0040-1951(81)90024-x
- Dai, L., & Karato, S. I. (2009). Electrical conductivity of pyrope-rich garnet at high temperature and high pressure. *Physics of the Earth and Planetary Interiors*, 176(1–2), 83–88. https://doi.org/10.1016/j.pepi.2009.04.002
- Dai, L., Li, H., Hu, H., Shan, S., Jiang, J., & Hui, K. (2012). The effect of chemical composition and oxygen fugacity on the electrical conductivity of dry and hydrous garnet at high temperatures and pressures. *Contributions to Mineralogy and Petrology*, 163(4), 689–700. https://doi.org/10.1007/s00410-011-0693-5
- Demouchy, S. (2010). Diffusion of hydrogen in olivine grain boundaries and implications for the survival of water-rich zones in the Earth's mantle. *Earth and Planetary Science Letters*, 295(1–2), 305–313. https://doi.org/10.1016/j.epsl.2010.04.019
- Eberhart-Phillips, D., Stanley, W. D., Rodriguez, B. D., & Lutter, W. J. (1995). Surface seismic and electrical methods to detect fluids related to faulting. *Journal of Geophysical Research: Solid Earth*, 100(B7), 12919–12936. https://doi.org/10.1029/94jb03256
- Evans, R. L., Hirth, G., Baba, K., Forsyth, D., Chave, A., & Mackie, R. (2005). Geophysical evidence from the MELT area for compositional controls on oceanic plates. *Nature*, 437(7056), 249–252. https://doi.org/10.1038/nature04014
- Fazzito, S. Y., Rapalini, A. E., Cortés, J. M., & Terrizzano, C. M. (2009). Characterization of Quaternary faults by electric resistivity tomography in the Andean Precordillera of Western Argentina. *Journal of South American Earth Sciences*, 28(3), 217–228. https://doi.org/10.1016/j. jsames.2009.06.001
- Ferrand, T. P. (2019a). Seismicity and mineral destabilizations in the subducting mantle up to 6 GPa, 200 km depth. *Lithos*, 334, 205–230. https://doi.org/10.1016/j.lithos.2019.03.014
- Ferrand, T. P. (2019b). Neither antigorite nor its dehydration is "metastable". American Mineralogist, 104(6), 788–790. https://doi.org/10.2138/am-2019-6957
- Ferrand, T. P. (2020). Conductive channels in the deep oceanic lithosphere could consist of garnet pyroxenites at the fossilized lithosphere—asthenosphere boundary. *Minerals*, 10(12), 1107. https://doi.org/10.3390/min10121107
- Ferrand, T. P., & Chin, E. (2023). Garnet pyroxenites explain high electrical conductivity in the East African deep lithosphere. *Lithos*, 462, 107405. https://doi.org/10.1016/j.lithos.2023.107405
- Ferrand, T. P., & Deldicque, D. (2021). Reduced viscosity of Mg<sub>2</sub>GeO<sub>4</sub> with minor MgGeO<sub>3</sub> between 1000 and 1150°C suggests solid-state lubrication at the lithosphere–asthenosphere boundary. *Minerals*, 11(6), 600. https://doi.org/10.3390/min11060600
- Ferrand, T. P., Hilairet, N., Incel, S., Deldicque, D., Labrousse, L., Gasc, J., et al. (2017). Dehydration-driven stress transfer triggers intermediate-depth earthquakes. *Nature Communications*, 8(1), 1–11. https://doi.org/10.1038/ncomms15247
- Ferrand, T. P., Labrousse, L., Eloy, G., Fabbri, O., Hilairet, N., & Schubnel, A. (2018). Energy balance from a mantle pseudotachylyte, Balmuccia, Italy. *Journal of Geophysical Research: Solid Earth*, 123(5), 3943–3967. https://doi.org/10.1002/2017jb014795

FERRAND ET AL. 19 of 22

15252027, 2025, 11, Downl

- Ferrand, T. P., Nielsen, S., Labrousse, L., & Schubnel, A. (2021). Scaling seismic fault thickness from the laboratory to the field. *Journal of Geophysical Research: Solid Earth*, 126(3), e2020JB020694. https://doi.org/10.1029/2020jb020694
- Ferrand, T. P., & Précigout, J. (2025). Database for "Electrical conductivity measurements during controlled deformation at upper-mantle conditions: First experimental achievements in a Griggs-type apparatus" [Dataset]. Zenodo. https://doi.org/10.5281/zenodo.14673136
- Fisher, J. C. (1951). Calculation of diffusion penetration curves for surface and grain boundary diffusion. *Journal of Applied Physics*, 22(1), 74–77. https://doi.org/10.1063/1.1699825
- Fisler, D. K., Mackwell, S. J., & Petsch, S. (1997). Grain boundary diffusion in enstatite. *Postgraduate Medicine*, 24(4), 264–273. https://doi.org/10.1007/s002690050038
- Fujinawa, Y., Takahashi, K., Noda, Y., Iitaka, H., & Yazaki, S. (2011). Remote detection of the electric field change induced at the seismic wave from the start of fault rupturing. In *IJG* 2011.
- Gaillard, F. (2004). Laboratory measurements of electrical conductivity of hydrous and dry silicic melts under pressure. Earth and Planetary Science Letters, 218(1–2), 215–228. https://doi.org/10.1016/s0012-821x(03)00639-3
- Gaillard, F., Malki, M., Iacono-Marziano, G., Pichavant, M., & Scaillet, B. (2008). Carbonatite melts and electrical conductivity in the asthenosphere. *Science*, 322(5906), 1363–1365. https://doi.org/10.1126/science.1164446
- Gardés, E., Gaillard, F., & Tarits, P. (2014). Toward a unified hydrous olivine electrical conductivity law. *Geochemistry, Geophysics, Geosystems*, 15(12), 4984–5000. https://doi.org/10.1002/2014gc005496
- Gasc, J., Gardonio, B., Deldicque, D., Daigre, C., Moarefvand, A., Petit, L., et al. (2022). Ductile vs. brittle strain localization induced by the olivine-ringwoodite transformation. *Minerals*, 12(6), 719. https://doi.org/10.3390/min12060719
- Girault, F., Adhikari, L. B., France-Lanord, C., Agrinier, P., Koirala, B. P., Bhattarai, M., et al. (2018). Persistent CO<sub>2</sub> emissions and hydrothermal unrest following the 2015 earthquake in Nepal. *Nature Communications*, 9(1), 2956. https://doi.org/10.1038/s41467-018-05138-z
- Girault, F., France-Lanord, C., Adhikari, L. B., Upreti, B. N., Paudyal, K. R., Gajurel, A. P., et al. (2023). Overview of hydrothermal systems in the Nepal Himalaya. *Himalaya: Dynamics of a Giant, Geodynamic Setting of the Himalayan Range*, 1, 225–254. https://doi.org/10.1002/0781204238894.abs
- Glover, P. W. J., Gomez, J. B., Meredith, P. G., Boon, S. A., Sammonds, P. R., & Murrell, S. A. F. (1996). Modelling the stress-strain behaviour of saturated rocks undergoing triaxial deformation using complex electrical conductivity measurements. *Surveys in Geophysics*, 17(3), 307–330. https://doi.org/10.1007/bf01904046
- Green, D. H., Hibberson, W. O., Kovács, I., & Rosenthal, A. (2010). Water and its influence on the lithosphere–asthenosphere boundary. *Nature*, 467(7314), 448–451. https://doi.org/10.1038/nature09369
- Green, H. W., & Borch, R. S. (1989). A new molten salt cell for precision stress measurements at high pressure. European Journal of Mineralogy, 1(2), 213–219.
- Green, H. W., & Houston, H. (1995). The mechanics of deep earthquakes. Annual Review of Earth and Planetary Sciences, 23(1), 169–214. https://doi.org/10.1146/annurev.ea.23.050195.001125
- Green, H. W., Young, T. E., Walker, D., & Scholz, C. H. (1990). Anticrack-associated faulting at very high pressure in natural olivine. *Nature*, 348(6303), 720–722. https://doi.org/10.1038/348720a0
- Griggs, D. (1967). Hydrolytic weakening of quartz and other silicates. *Geophysical Journal International*, 14(1–4), 19–31. https://doi.org/10.1111/j.1365-246x.1967.tb06218.x
- Hansen, L. N., Zimmerman, M. E., & Kohlstedt, D. L. (2012). The influence of microstructure on deformation of olivine in the grain-boundary sliding regime. *Journal of Geophysical Research: Solid Earth*, 117(B9), B09201, https://doi.org/10.1029/2012jb009305
- Hill, G. J., Caldwell, T. G., Heise, W., Chertkoff, D. G., Bibby, H. M., Burgess, M. K., et al. (2009). Distribution of melt beneath Mount St Helens and Mount Adams inferred from magnetotelluric data. *Nature Geoscience*, 2(11), 785–789. https://doi.org/10.1038/ngeo661
- Hiraga, T., Anderson, I. M., & Kohlstedt, D. L. (2004). Grain boundaries as reservoirs of incompatible elements in the Earth's mantle. *Nature*, 427(6976), 699–703. https://doi.org/10.1038/nature02259
- Hirth, G., & Kohlstedt, D. L. (1996). Water in the oceanic upper mantle: Implications for rheology, melt extraction and the evolution of the lithosphere. *Earth and Planetary Science Letters*, 144(1–2), 93–108. https://doi.org/10.1016/0012-821x(96)00154-9
- Holtzman, B. K., & Kendall, J. M. (2010). Organized melt, seismic anisotropy, and plate boundary lubrication. Geochemistry, Geophysics, Geosystems, 11(12), Q0AB06. https://doi.org/10.1029/2010gc003296
- Holtzman, B. K., Kohlstedt, D. L., Zimmerman, M. E., Heidelbach, F., Hiraga, T., & Hustoft, J. (2003). Melt segregation and strain partitioning: Implications for seismic anisotropy and mantle flow. Science, 301(5637), 1227–1230. https://doi.org/10.1126/science.1087132
- Holyoke, C. W., III, & Kronenberg, A. K. (2010). Accurate differential stress measurement using the molten salt cell and solid salt assemblies in the Griggs apparatus with applications to strength, piezometers and rheology. *Tectonophysics*, 494(1–2), 17–31. https://doi.org/10.1016/j.tecto. 2010 08 001
- Ingham, M., & Brown, C. (1998). A magnetotelluric study of the Alpine Fault, New Zealand. Geophysical Journal International, 135(2), 542–552. https://doi.org/10.1046/j.1365-246x.1998.00659.x
- Jackson, İ., Paterson, M. S., & Fitz Gerald, J. D. (1992). Seismic wave dispersion and attenuation in Åheim dunite: An experimental study. Geophysical Journal International, 108(2), 517–534. https://doi.org/10.1111/j.1365-246x.1992.tb04633.x
- Jiracek, G. R., Gonzalez, V. M., Caldwell, T. G., Wannamaker, P. E., & Kilb, D. (2007). Seismogenic, electrically conductive, and fluid zones at continental plate boundaries in New Zealand, Himalaya, and California, USA. AGU Geophysical Monograph, 175, 347.
- Johannes, W., & Puhan, D. (1971). The calcite-aragonite transition, reinvestigated. Contributions to Mineralogy and Petrology, 31(1), 28–38. https://doi.org/10.1007/bf00373389
- Jouniaux, L., Zamora, M., & Reuschlé, T. (2006). Electrical conductivity evolution of non-saturated carbonate rocks during deformation up to failure. *Geophysical Journal International*, 167(2), 1017–1026.
- Karaş, M., Tank, S. B., Ogawa, Y., Oshiman, N., Matsushima, M., & Honkura, Y. (2020). Probing the relationship between electrical conductivity and creep through upper crustal fluids along the western part of the North Anatolian Fault with three-dimensional magnetotellurics. *Tecto-nophysics*, 791, 228561. https://doi.org/10.1016/j.tecto.2020.228561
- Karaş, M., Tank, S. B., & Özaydın, S. (2017). Electrical conductivity of a locked fault: Investigation of the Ganos segment of the North Anatolian Fault using three-dimensional magnetotellurics. Earth Planets and Space, 69, 1–14.
- Karato, S. I. (1990). The role of hydrogen in the electrical conductivity of the upper mantle. *Nature*, 347(6290), 272–273. https://doi.org/10.1038/347272a0
- Karato, S. I. (2006). Influence of hydrogen-related defects on the electrical conductivity and plastic deformation of mantle minerals: A critical review. AGU Geophysical Monograph, 168, 113–129. https://doi.org/10.1029/168gm09
- Kawakatsu, H., Kumar, P., Takei, Y., Shinohara, M., Kanazawa, T., Araki, E., & Suyehiro, K. (2009). Seismic evidence for sharp lithosphere-asthenosphere boundaries of oceanic plates. *Science*, 324(5926), 499–502. https://doi.org/10.1126/science.1169499

FERRAND ET AL. 20 of 22

- Kawano, S., Yoshino, T., & Katayama, I. (2012). Electrical conductivity of magnetite-bearing serpentinite during shear deformation. Geophysical Research Letters, 39(20), 762. https://doi.org/10.1029/2012g1053652
- Kaya, T., Kasaya, T., Tank, S. B., Ogawa, Y., Tunçer, M. K., Oshiman, N., et al. (2013). Electrical characterization of the North Anatolian Fault Zone underneath the Marmara Sea, Turkey by ocean bottom magnetotellurics. *Geophysical Journal International*, 193(2), 664–677. https://doi. org/10.1093/gji/ggt025
- Key, K., Constable, S., Liu, L., & Pommier, A. (2013). Electrical image of passive mantle upwelling beneath the northern East Pacific Rise. Nature, 495(7442), 499–502. https://doi.org/10.1038/nature11932
- Kido, M., Muto, J., & Nagahama, H. (2016). Method for correction of differential stress calculations from experiments using the solid salt assembly in a Griggs-type deformation apparatus. *Tectonophysics*, 672, 170–176. https://doi.org/10.1016/j.tecto.2016.02.011
- Kluge, E. K., Toy, V., & Lockner, D. (2022). Electrical properties and anisotropy of schists and fault rocks from New Zealand's Southern Alps under confining pressure. *Geosciences*, 12(3), 121. https://doi.org/10.3390/geosciences12030121
- Laumonier, M., Farla, R., Frost, D. J., Katsura, T., Marquardt, K., Bouvier, A. S., & Baumgartner, L. P. (2017). Experimental determination of melt interconnectivity and electrical conductivity in the upper mantle. *Earth and Planetary Science Letters*, 463, 286–297. https://doi.org/10.1016/j.epsl.2017.01.037
- Lazari, F., Meyer, G., & Violay, M. (2024). Effects of pore fluid chemistry on the localized to ductile transition of sandstone. In EGU abstract EGU24-15531.
- Lemonnier, C., Marquis, G., Perrier, F., Avouac, J. P., Chitrakar, G., Kafle, B., et al. (1999). Electrical structure of the Himalaya of central Nepal: High conductivity around the mid-crustal ramp along the MHT. *Geophysical Research Letters*, 26(21), 3261–3264. https://doi.org/10.1029/1999g1008363
- Le Roux, P. J., Shirey, S. B., Hauri, E. H., Perfit, M. R., & Bender, J. F. (2006). The effects of variable sources, processes and contaminants on the composition of northern EPR MORB (8–10 N and 12–14 N): Evidence from volatiles (H<sub>2</sub>O, CO<sub>2</sub>, S) and halogens (F, Cl). Earth and Planetary Science Letters, 251(3–4), 209–231.
- Li, S., Li, J., Ferrand, T. P., Zhou, T., Lv, M., Xi, Z., et al. (2023). Deep geophysical anomalies beneath the Changbaishan volcano. *Journal of Geophysical Research: Solid Earth*, 128(4), e2022JB025671. https://doi.org/10.1029/2022jb025671
- Li, S., Unsworth, M. J., Booker, J. R., Wei, W., Tan, H., & Jones, A. G. (2003). Partial melt or aqueous fluid in the mid-crust of Southern Tibet?

  Constraints from INDEPTH magnetotelluric data. *Geophysical Journal International*, 153(2), 289–304. https://doi.org/10.1046/j.1365-246x.
- Mansard, N., Raimbourg, H., Augier, R., Précigout, J., & Le Breton, N. (2018). Large-scale strain localization induced by phase nucleation in midcrustal granitoids of the south Armorican massif. *Tectonophysics*, 745, 46–65. https://doi.org/10.1016/j.tecto.2018.07.022
- Mantisi, B., Sator, N., & Guillot, B. (2017). Structure and transport at grain boundaries in polycrystalline olivine: An atomic-scale perspective. Geochimica et Cosmochimica Acta, 219, 160–176. https://doi.org/10.1016/j.gca.2017.09.026
- Marquardt, K., & Faul, U. H. (2018). The structure and composition of olivine grain boundaries: 40 years of studies, status and current developments. *Physics and Chemistry of Minerals*, 45(2), 139–172. https://doi.org/10.1007/s00269-017-0935-9
- Martí, A., Queralt, P., Marcuello, A., Ledo, J., Rodríguez-Escudero, E., Martínez-Díaz, J. J., et al. (2020). Magnetotelluric characterization of the Alhama de Murcia Fault (Eastern Betics, Spain) and study of magnetotelluric interstation impedance inversion. *Earth Planets and Space*, 72(1), 16. https://doi.org/10.1186/s40623-020-1143-2
- Masana, E., Martínez-Díaz, J. J., Hernández-Enrile, J. L., & Santanach, P. (2004). The Alhama de Murcia fault (SE Spain), a seismogenic fault in a diffuse plate boundary: Seismotectonic implications for the Ibero-Magrebian region. *Journal of Geophysical Research: Solid Earth*, 109(B1), B01301. https://doi.org/10.1029/2002jb002359
- Mazzella, A., & Morrison, H. F. (1974). Electrical resistivity variations associated with earthquakes on the San Andreas fault. *Science*, 185(4154), 855–857. https://doi.org/10.1126/science.185.4154.855
- Mirwald, P. W. (1979). The electrical conductivity of calcite between 300 and 1200° C at a CO<sub>2</sub> pressure of 40 bars. *Physics and Chemistry of Minerals*. 4(4), 291–297. https://doi.org/10.1007/bf00307532
- Moarefvand, A., Gasc, J., Fauconnier, J., Baïsset, M., Burdette, E., Labrousse, L., & Schubnel, A. (2021). A new-generation Griggs apparatus with active acoustic monitoring. *Tectonophysics*, 816, 229032. https://doi.org/10.1016/j.tecto.2021.229032
- Naif, S., Key, K., Constable, S., & Evans, R. L. (2013). Melt-rich channel observed at the lithosphere–asthenosphere boundary. *Nature*, 495(7441), 356–359. https://doi.org/10.1038/nature11939
- Niu, Y., Regelous, M., Wendt, I. J., Batiza, R., & O'Hara, M. J. (2002). Geochemistry of near-EPR seamounts: Importance of source vs. process and the origin of enriched mantle component. *Earth and Planetary Science Letters*, 199(3–4), 327–345. https://doi.org/10.1016/s0012-821x (02)00591-5
- Novella, D., Jacobsen, B., Weber, P. K., Tyburczy, J. A., Ryerson, F. J., & Du Frane, W. L. (2017). Hydrogen self-diffusion in single crystal olivine and electrical conductivity of the earth's mantle. *Scientific Reports*, 7(1), 5344. https://doi.org/10.1038/s41598-017-05113-6
- Ono, S., & Mibe, K. (2015). Influence of pressure and temperature on the electrical conductivity of dolomite. *Physics and Chemistry of Minerals*, 42(9), 773–779. https://doi.org/10.1007/s00269-015-0761-x
- Paterson, M. S., & Olgaard, D. L. (2000). Rock deformation tests to large shear strains in torsion. *Journal of Structural Geology*, 22(9), 1341–1358. https://doi.org/10.1016/s0191-8141(00)00042-0
- Pieri, M., Burlini, L., Kunze, K., Stretton, I., & Olgaard, D. L. (2001). Rheological and microstructural evolution of Carrara marble with high shear strain: Results from high temperature torsion experiments. *Journal of Structural Geology*, 23(9), 1393–1413. https://doi.org/10.1016/s0191-8141(01)00006-2
- Pommier, A., Kohlstedt, D. L., Hansen, L. N., Mackwell, S., Tasaka, M., Heidelbach, F., & Leinenweber, K. (2018). Transport properties of olivine grain boundaries from electrical conductivity experiments. *Contributions to Mineralogy and Petrology*, 173(5), 1–13. https://doi.org/10.1007/s00410-018-1468-z
- Précigout, J., Ledoux, E., Arbaret, L., & Spriet, C. (2022). Porosity induced by dislocation dynamics in quartz-rich shear bands of granitic rocks. Scientific Reports, 12(1), 6141. https://doi.org/10.1038/s41598-022-10053-x
- Précigout, J., Prigent, C., Palasse, L., & Pochon, A. (2017). Water pumping in mantle shear zones. *Nature Communications*, 8(1), 1–10. https://doi.org/10.1038/ncomms15736
- Précigout, J., & Stünitz, H. (2016). Evidence of phase nucleation during olivine diffusion creep: A new perspective for mantle strain localisation. Earth and Planetary Science Letters, 455, 94–105. https://doi.org/10.1016/j.epsl.2016.09.029
- Précigout, J., Stünitz, H., Pinquier, Y., Champallier, R., & Schubnel, A. (2018). High-pressure, high-temperature deformation experiment using the new generation Griggs-type apparatus. *Journal of Visualized Experiments*, 134, e56841. https://doi.org/10.3791/56841
- Précigout, J., Stünitz, H., & Villeneuve, J. (2019). Excess water storage induced by viscous strain localization during high-pressure shear experiment. *Scientific Reports*, 9(1), 1–9. https://doi.org/10.1038/s41598-019-40020-y

FERRAND ET AL. 21 of 22

- Proctor, B., & Hirth, G. (2016). "Ductile to brittle" transition in thermally stable antigorite gouge at mantle pressures. *Journal of Geophysical Research: Solid Earth*, 121(3), 1652–1663. https://doi.org/10.1002/2015jb012710
- Ritter, O., Hoffmann-Rothe, A., Bedrosian, P. A., Weckmann, U., & Haak, V. (2005). Electrical conductivity images of active and fossil fault zones. *Geological Society*, 245(1), 165–186. https://doi.org/10.1144/gsl.sp.2005.245.01.08
- Rybacki, E., Evans, B., Janssen, C., Wirth, R., & Dresen, G. (2013). Influence of stress, temperature, and strain on calcite twins constrained by deformation experiments. *Tectonophysics*, 601, 20–36. https://doi.org/10.1016/j.tecto.2013.04.021
- Rybacki, E., Niu, L., & Evans, B. (2021). Semi-brittle deformation of Carrara marble: Hardening and twinning induced plasticity. *Journal of Geophysical Research: Solid Earth*, 126(12), e2021JB022573. https://doi.org/10.1029/2021jb022573
- Rychert, C. A., Harmon, N., Constable, S., & Wang, S. (2020). The nature of the lithosphere-asthenosphere boundary. *Journal of Geophysical Research: Solid Earth*, 125(10), e2018JB016463. https://doi.org/10.1029/2018jb016463
- Schmerr, N. (2012). The Gutenberg discontinuity: Melt at the lithosphere-asthenosphere boundary. Science, 335(6075), 1480–1483. https://doi.org/10.1126/science.1215433
- Shen, K., Wang, D., Wang, L., Yi, L., Zhang, Z., & Cao, C. (2023). Electrical conductivity of clinochlore dehydration and implications for high-conductivity anomalies and the melting in the mantle wedge. *Journal of Geophysical Research: Solid Earth*, 128(8), e2022JB025722. https://doi.org/10.1029/2022jb025722
- Sifré, D., Gardés, E., Massuyeau, M., Hashim, L., Hier-Majumder, S., & Gaillard, F. (2014). Electrical conductivity during incipient melting in the oceanic low-velocity zone. *Nature*, 509(7498), 81–85. https://doi.org/10.1038/nature13245
- Sommer, H., Regenauer-Lieb, K., Gasharova, B., & Siret, D. (2008). Grain boundaries: A possible water reservoir in the Earth's mantle? Mineralogy and Petrology, 94(1–2), 1–8. https://doi.org/10.1007/s00710-008-0002-9
- Staudigel, H., & Schreyer, W. (1977). The upper thermal stability of clinochlore, Mg<sub>5</sub>Al[AlSi<sub>3</sub>O<sub>10</sub>](OH)<sub>8</sub>, at 10-35 kb P<sub>H2O</sub>. Contributions to Mineralogy and Petrology, 61(2), 187–198. https://doi.org/10.1007/bf00374367
- Stern, T. A., Henrys, S. A., Okaya, D., Louie, J. N., Savage, M. K., Lamb, S., et al. (2015). A seismic reflection image for the base of a tectonic plate. *Nature*, 518(7537), 85–88. https://doi.org/10.1038/nature14146
- Sun, W., Jiang, J., Dai, L., Hu, H., Wang, M., Qi, Y., & Li, H. (2021). Electrical properties of dry polycrystalline olivine mixed with various chromite contents: Implications for the high conductivity anomalies in subduction zones. *Geoscience Frontiers*, 12(5), 101178. https://doi.org/ 10.1016/j.gsf.2021.101178
- Takei, Y., & Holtzman, B. K. (2009). Viscous constitutive relations of solid-liquid composites in terms of grain boundary contiguity: 3. Causes and consequences of viscous anisotropy. *Journal of Geophysical Research*, 114(B6). https://doi.org/10.1029/2008jb005852
- Ten Grotenhuis, S. M., Drury, M. R., Peach, C. J., & Spiers, C. J. (2004). Electrical properties of fine-grained olivine: Evidence for grain boundary transport. *Journal of Geophysical Research: Solid Earth*, 109(B6), 1–9. https://doi.org/10.1029/2003jb002799
- Thieme, M., Demouchy, S., Barou, F., Beausir, B., Taupin, V., & Cordier, P. (2023). Dislocation and disclination densities in experimentally deformed polycrystalline olivine. *European Journal of Mineralogy*, 35(2), 219–236. https://doi.org/10.5194/ejm-35-219-2023
- deformed polycrystalline offvine. European Journal of Mineralogy, 35(2), 219–236. https://doi.org/10.5194/ejm-35-219-2023
  Tullis, T. E., & Tullis, J. (1986). Experimental rock deformation techniques. In Mineral and rock deformation: Laboratory studies (Vol. 36, pp.
- 297–324). https://doi.org/10.1029/gm036p0297
  Türkoğlu, E., Unsworth, M., Bulut, F., & Çağlar, İ. (2015). Crustal structure of the North Anatolian and East Anatolian Fault Systems from
- magnetotelluric data. *Physics of the Earth and Planetary Interiors*, 241, 1–14. https://doi.org/10.1016/j.pepi.2015.01.003

  Türkoğlu, E., Unsworth, M., Çağlar, İ., Tuncer, V., & Avşar, Ü. (2008). Lithospheric structure of the Arabia-Eurasia collision zone in eastern Anatolia: Magnetotelluric evidence for widespread weakening by fluids? *Geology*, 36(8), 619–622. https://doi.org/10.1130/g24683a.1
- Unsworth, M. (2010). Magnetotelluric studies of active continent–continent collisions. Surveys in Geophysics, 31(2), 137–161. https://doi.org/10.1007/s10712-009-9086-y
- Unsworth, M. J., Jones, A. G., Wei, W., Marquis, G., Gokarn, S. G., Spratt, J. E., & Indepth-MT team (2005). Crustal rheology of the Himalaya and Southern Tibet inferred from magnetotelluric data. *Nature*, 438(7064), 78–81. https://doi.org/10.1038/nature04154
- Wheeler, J., Kohlstedt, D. L., & Evans, B. (2001). Grain boundary sliding in olivine. *Geophysical Research Letters*, 28(4), 611–614.
- Xu, S., Unsworth, M. J., Hu, X., & Mooney, W. D. (2019). Magnetotelluric evidence for asymmetric simple shear extension and lithospheric thinning in South China. *Journal of Geophysical Research: Solid Earth*, 124(1), 104–124. https://doi.org/10.1029/2018jb016505
- Yamauchi, H., & Takei, Y. (2020). Application of a premelting model to the Lithosphere-Asthenosphere boundary. Geochemistry, Geophysics, Geosystems, 21(11), e2020GC009338. https://doi.org/10.1029/2020gc009338
- Yoshino, T. (2010). Laboratory electrical conductivity measurement of mantle minerals. Surveys in Geophysics, 31(2), 163–206. https://doi.org/10.1007/s10712-009-9084-0
- Yoshino, T., Laumonier, M., McIsaac, E., & Katsura, T. (2010). Electrical conductivity of basaltic and carbonatite melt-bearing peridotites at high pressures: Implications for melt distribution and melt fraction in the upper mantle. *Earth and Planetary Science Letters*, 295(3–4), 593–602. https://doi.org/10.1016/j.eps1.2010.04.050
- Zhang, B., & Yoshino, T. (2020). Temperature-enhanced electrical conductivity anisotropy in partially molten peridotite under shear deformation. Earth and Planetary Science Letters, 530, 115922. https://doi.org/10.1016/j.epsl.2019.115922
- Zhang, B., Yoshino, T., Yamazaki, D., Manthilake, G., & Katsura, T. (2014). Electrical conductivity anisotropy in partially molten peridotite under shear deformation. *Earth and Planetary Science Letters*, 405, 98–109. https://doi.org/10.1016/j.epsl.2014.08.018
- Zhu, T., Feng, R., Hao, J. Q., Zhou, J. G., Wang, H. L., & Wang, S. Q. (2009). The application of electrical resistivity tomography to detecting a buried fault: A case study. *Journal of Environmental & Engineering Geophysics*, 14(3), 145–151. https://doi.org/10.2113/jeeg14.3.145

FERRAND ET AL. 22 of 22